Chapter 6
High Wind Speed Regime

Abstract Under high wind speed conditions breaking waves disrupt the air-sea interface producing a two-phase zone—air bubbles in water and sea spray in air. This mixed-phase environment changes the regime of air-sea interaction. In this chapter, after reviewing dynamics of air-bubbles and sea spray droplets in detail, the reader is exposed to the idea that under strong winds Kelvin-Helmholtz instability is the likely mechanism for the intense production of spume and formation of a two-phase transition layer. The resulting two-phase environment eliminates short wind-waves, including some responsible for a substantial part of the surface wind stress. Amazingly, this concept provides an explanation for the rapid intensification of some storms to major tropical cyclones and observed bi-modal distribution of tropical cyclone maximum intensity. A long overdue implementation of sea surface micro-physics into operational models is expected to improve predictions of tropical cyclone intensity and the associated wave field.

Keywords Whitecaps • Sea spray • Spume • Air bubbles • Marine aerosol • Drag coefficient • Kelvin-Helmholtz instability • Tollmien-Schlichting instability • Two-phase environment • Transition layer

6.1 Introduction

With increasing wind speed, the sharp interface between the air and water disappears for longer intervals and over larger area (Fig. 6.1). Under high winds, the concept of the air-sea interface becomes problematic. A two-phase environment with transition from bubble-filled water to spray-filled air is formed. In very high winds, a distinct layer of foam is observed.

The effects of bubbles and sea spray appear to be of crucial importance for air–sea exchanges in tropical cyclones. In particular, modification of short surface waves by two-phase environment may have appreciable consequences for the air–sea drag coefficient. These effects can also be important for extratropical winter storms.

In Sect. 6.1 of this chapter, we consider air bubbles in the near-surface layer of the ocean. Effects of the bubbles produced by breaking surface waves include the modification of upper ocean turbulence by rising bubbles, their contribution to

A. Soloviev, R. Lukas, *The Near-Surface Layer of the Ocean,* Atmospheric and Oceanographic Sciences Library 48, DOI 10.1007/978-94-007-7621-0_6,

air–sea gas exchange, and to the acoustic and optical environments. Sea spray and marine aerosol generation is the subject of Sect. 6.2. Section 6.3 discusses the issues of modeling air–sea exchanges in high wind conditions and intends to explain the recently discovered phenomenon of the limiting state of the aerodynamic roughness under hurricane conditions. Section 6 concludes this chapter.

6.2 Air Bubbles in the Near-Surface Turbulent Boundary Layer

6.2.1 Active and Passive Phases in Bubble Life

The high wind speed regime is associated with energetic wave-breaking events. The fraction of the ocean surface covered with wave breakers rapidly increases with wind speed though, according to recent data, does not seem to exceed 10 % even under very strong winds (Holthuijsen et al. 2012).

Breaking waves entrain air and create bubble plumes, which are highly transient and localized phenomena. Based on laboratory experiments of Leifer and de Leeuw (2001), the lifetime of wave-generated bubbles can be divided into four phases (1) formation, (2) injection, (3) rise, and (4) senescence. The first phase is observed to occur during the first 0.1 s or less. During the second phase, the plume rapidly descends, initially at roughly a 30° angle, then tilting toward the vertical. The second (injection) phase ends at the maximum penetration depth; it is followed by the third phase, when the mass of bubbles rises toward the surface. The injection and rise phases last roughly the same time. Once the bubble creation process ceases, a newly formed bubble plume becomes acoustically quiescent and evolves under the influence of turbulent diffusion, advection, buoyant degassing, and dissolution. This is the fourth, senescence, phase, which corresponds to typical bubble observations (that is the background distribution). During the senescence phase the plume consists of the smaller, mostly $r < 0.2$ mm bubbles.

Size-dependent bubble rise velocity mainly determines the residence time of larger bubbles, but the residence time of smaller bubbles may also be affected by the turbulent flow in the near-surface layer. Bubble plumes consisting of small bubbles can extend well into the mixed layer. As a result, the smaller bubbles act as tracers and map out the surface signatures of Langmuir cells (Farmer and Li 1995), or the edges of current fronts and rips (Marmorino and Trump 1996).

6.2.2 Bubble Rise Velocity

Bubble hydrodynamics depend on bubble size, temperature, and the presence of surfactants (Leifer et al. 2000). Depending on size, the bubble form varies from

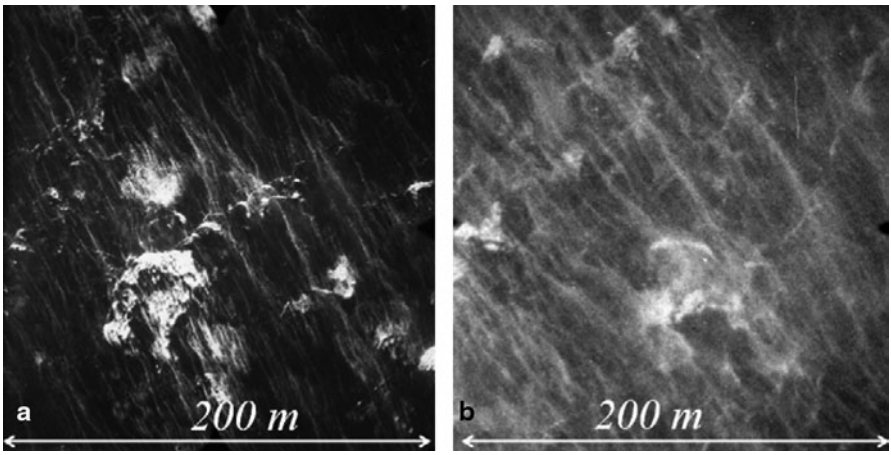

Fig. 6.1 Ocean surface foam streaks observed on photographic images of the sea surface in a hurricane: **a** Wind speed 28 m s^{-1} and **b** wind speed 46 m s^{-1}. After Black et al. (2006)

spherical to spheroid for small bubbles ($r<0.5$ mm) to ellipsoid for larger bubbles ($r>0.5$ mm). The radius of transition between the spheroidal and ellipsoidal form depends on the temperature and on the presence of surfactants. Small bubbles are nearly perfect spheres because surface tension dominates over the drag stress that acts upon the rising bubble. The surface tension force, however, decreases inversely proportional to the bubble radius. At the same time, the drag force increases since larger bubbles rise faster and have larger effective cross-sectional area. Bubbles with radius larger than approximately 0.7 mm (at $T=20°C$) can oscillate, in both path and shape, affecting the rise velocity. The trajectory oscillations (zigzag or helical) are important for bubbles that just start oscillating and reduce their speed. For large bubbles ($r>3.5$ mm), the shape or deformation oscillations are more important. The latter results in the reduction of the drag coefficient and thus an increase of rise speed.

The important factor in bubble hydrodynamics is the presence of surfactants, which can partially immobilize the surface, increasing drag and decreasing rise velocity. In the bubble radii range from approximately 0.25 mm to 10 mm, clean bubbles have different hydrodynamics from *dirty* (i.e., surfactant covered) bubbles.

Thorpe (1982) proposed a formula for the buoyant rise speed of bubbles:

$$w_b(r)=\left(\frac{2r^2g}{9\nu}\right)\left[\left(y^2+2y\right)^{1/2}-y\right] \tag{6.1}$$

where $y=10.82\nu^2/\left(gr^3\right)$. This equation is derived for dirty bubbles (small bubbles become covered with surfactants within a short time period).

Patro et al. (2001) proposed an analytical parameterization formula for clean non-oscillating bubbles:

Table 6.1 Coefficients for Eq. (6.2) parameterizing the rise velocity for clean non-oscillating bubbles. (After Patro et al. 2001)

Re	r (μm)	c	d	n
<1	<60	0.666	2.0	−1.00
1–150	60–500	0.139	1.372	−0.64
150–420	550–660	11.713	2.851	−0.64
420–470	660–700	0.156	1.263	−0.64
470–540	700–850	0.021	0.511	−0.64

Table 6.2 Coefficients for Eq. (6.3) parameterizing clean oscillating bubbles. (After Patro et al. 2001)

H_1	K_1	r_C	w_{bm}	m_1	m_2
-4.792×10^{-4}	0.733	0.0584	22.16	−0.849	−0.815

$$w_b = \frac{c}{3} g r^d v^n \tag{6.2}$$

where the coefficients c, d, and n for this equation are given in Table 6.1.

For clean oscillating bubbles, Patro et al. (2001) developed the following analytic parameterization:

$$w_b = \left[w_{bm} + H_1 \left(r - r_c \right)^{m_1} \right] \exp\left[K_1 \left(r - r_c \right)^{m_2 T} \right] \tag{6.3}$$

where the coefficients H, K, m_1, and m_2 and the critical radius r_C (below which the parameterization suggests that bubbles do not oscillate for any temperature T), and the minimum velocity w_{bm} for oscillating bubbles are given in Table 6.2. Parameterization (6.3) is applicable for oscillating bubbles for $0\,^0\mathrm{C} < T < 30\,^0\mathrm{C}$ and $r_p < r < 4$ mm. The radius r for the onset of oscillation varies with temperature T according to the parameterization relationship,

$$r_p = 1086 - 16.05\, T_p \tag{6.4}$$

where r_p and T_p are the peak radius and temperature, respectively.

A comparison of observed bubble rise velocities in clean and natural waters is shown in Fig. 6.2, together with the parameterizations for clean and dirty bubbles (Clift et al. 1978). The parameterization for clean bubbles demonstrates a monotonic increase of w_b with radius r until the onset of oscillation, after which w_b decreases to some level and then starts increasing again. In contrast, the parameterization for dirty bubbles shows a monotonic increase with r.

The observational data given by Clift et al. (1978) suggest that the rise velocity for seawater bubbles with radii larger than approximately 0.6 mm is close to that of hydrodynamically clean bubbles. An explanation is that larger bubbles rise quickly to the surface and thus do not have sufficient time to collect surfactants (Keeling

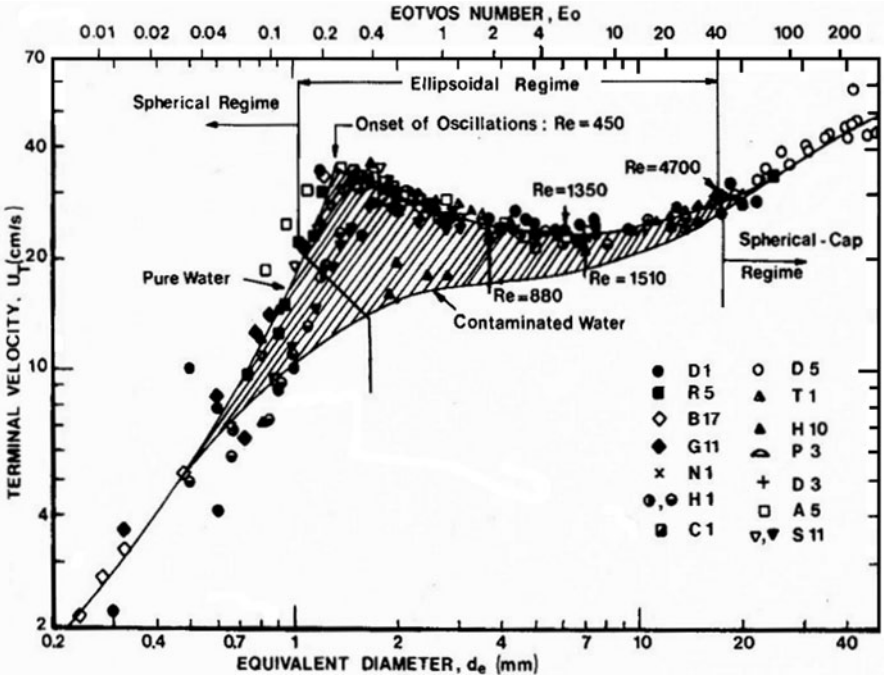

Fig. 6.2 The bubble rise velocity for hydrodynamically clean and dirty bubbles as a function of the bubble size. After Clift et al. (1978)

1993; Woolf 1993). Small bubbles (less than approximately 0.3 mm radius) are assumed to perform hydrodynamically as dirty bubbles (Woolf and Thorpe 1991). Their surface becomes covered with surfactants almost instantaneously.

Patro et al. (2001) proposed to treat small bubbles in seawater as dirty and large bubbles as clean with a transition at circa 0.6 mm. The transition radius somewhat increases with the increase of the bubble residence time in the water column. The assumption about clean and dirty bubbles is, however, somewhat uncertain. Adding to the uncertainty is the interaction among bubbles and their collective behavior in bubble clouds.

The presence of a persistent air bubble layer near the surface depends on the terminal velocity of bubbles, w_b, and the root mean square (RMS) vertical turbulence velocity, w_{RMS}. When $w_b < w_{RMS}$. The bubbles may remain in suspension for a timescale comparable to the average time interval between wave-breaking events at that location, thus forming a persistent background air bubble layer (Deane 2012). According to Deane's estimate, for winds above 13 m s^{-1}, the flat bubble terminal velocity dependence results in a rapid increase in the size of bubbles in the near-surface layer, leading to acoustic screening of the ocean surface from below by bubbles.

6.2.3 Bubble Size Distribution Function

The bubble-mediated component of air–sea gas exchanges, production of spray droplets and aerosols, optical properties of the sea surface, generation of ambient noise and sound transmission within the oceans, and scavenging of biological surfactants essentially depend on the size distribution of bubbles. The size distribution of entrained bubbles is also an important factor in controlling turbulence and dynamics in wave breakers. In addition, bubbles of different sizes behave differently in the turbulent surface layer. Bubble size distribution data potentially lead to a dynamical description of air–sea interaction based on near-surface turbulence, advection, and other properties.

Different approaches for measuring bubble size spectra, from acoustical to optical, have been developed. Each technique has advantages and disadvantages and is effective over different size ranges and bubble density regimes (Leifer et al. 2003). Acoustic methods have played a definite role in observing bubble size distributions because bubbles have a high resonance quality factor leading to an acoustical cross section some three orders of magnitude greater than their geometrical cross section (Farmer et al 1998). This effect reaches a maximum typically around a frequency of 30 kHz, which corresponds to a bubble radius of 100 μm. Different sound frequencies excite bubbles of different radii, which allow an estimate of the bubble size distribution from acoustic measurements. However, acoustic methods have difficulties with large bubbles ($r > 0.5$–0.7 mm), which are nonspherical in turbulent flow, and for high bubble concentrations. Laser techniques are noninvasive but, in common with acoustic methods, have problems when multiple bubbles enter the beam (high bubble density) and with large bubbles ($r > 1$ mm), whose mean shape is elliptical and is subject to oscillations. The optical methods based on the analysis of video or photo images are able to measure at high bubble concentrations and over a wide range of bubble sizes. The optical methods are, however, invasive in general and may disturb the measurement area.

The initial bubble formation, breakup, coalescence, dissolution, vertical motion caused by buoyancy forces, and turbulent mixing are the processes that determine the bubble size distribution in the ocean. Air is initially entrained into relatively large bubbles as a wave breaks. These bubbles rapidly break into smaller bubbles. During this active phase the bubble fragmentation process determines the bubble size distribution. Breaking waves directly inject air into the wave-stirred layer (see Fig. 3.1). As soon as the wave breaker expends its energy, the air entrainment ceases and the bubble creation process stops. The bubble size distribution then evolves rapidly because larger bubbles leave the area and surface more quickly than smaller ones.

The bubbles with radius $r > 0.7$ mm have rising velocities of the order of 0.2 m s^{-1}–0.4 m s^{-1} (Fig. 6.2); after the end of the wave-breaking process the remaining turbulence has little effect on their dynamics. The large bubbles immediately return to the surface, rarely penetrating below the wave-stirred layer. Note that the wave-stirred layer depth is typically less than one significant wave height (see

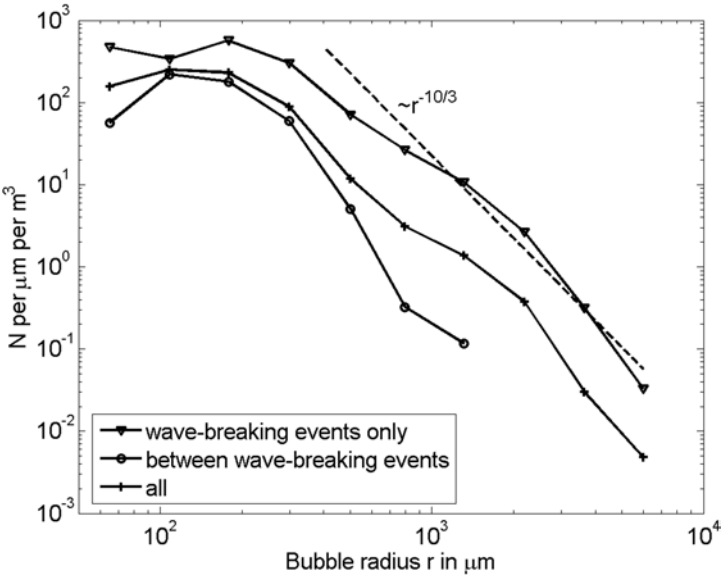

Fig. 6.3 Bubble size distributions at 0.6 m depth including and excluding wave-breaking events (Bowyer 2001). These measurements are taken at 11–13 m s^{-1} wind speed, 2.5 m wave height, and 15–120 km fetch. Reproduced by permission of American Geophysical Union

Chap. 3, Fig. 3.19). Smaller bubbles ($r \sim 0.1$ mm) have terminal velocities of the order of 0.01 m s^{-1}. The background turbulence as well as organized structures (see Chap. 5) can transport these small bubbles to greater depths.

The bubble size spectra can be separated into the regions within the wave-stirred layer and below the wave-stirred layer. The spectra within the wave-stirred layer can additionally be separated into those taken during wave-breaking events and those in between wave-breaking events.

Figure 6.3 shows averaged bubble spectra measured at 0.6 m depth including and excluding wave-breaking events. These observations are presumably in the wave-stirred layer. The density of bubbles, especially of large bubbles, is significantly higher during wave-breaking events. In this example, the slope of the spectrum for large bubbles changes in logarithmic coordinates from approximately −2.9 during wave-breaking events to approximately −4.3 between the wave-breaking events.

Two mechanisms for large bubble fragmentation are possible in the wave breaker: (1) turbulent fragmentation represented by the turbulent kinetic energy dissipation rate ε and (2) rising-bubble fragmentation, characterized by the rising velocity w_b and the collective behavior of rising bubbles.

From dimensional considerations, Garrett et al. (2000) derived a bubble size spectrum for the turbulent fragmentation mechanism

$$N(r) \propto Q\varepsilon^{-1/3} r^{-10/3} \tag{6.5}$$

where $N(r)$ is the number of bubbles per m^3 per mm radius increment (bubble density), Q is the volume of air entrained per volume of water per second (with dimension s^{-1}), and r is the bubble radius. The turbulent fragmentation mechanism is important during wave-breaking events. A theoretical spectrum (6.5) is compared in Fig. 6.3 with the field data of Bowyer (2001). For bubbles larger than approximately 1 mm, the slope of the theoretical spectrum is, in fact, consistent with the experimental spectrum averaged over wave-breaking events.

Spectrum (6.5) is based on the concept of turbulent fragmentation formulated by Kolmogorov (1949) and Hinze (1955). They pointed out that at high Reynolds number, a droplet of any different fluid or a gas bubble is likely to break up under the influence of differential pressure forces on its surface if these forces exceed the restoring forces of surface tension. Turbulent fragmentation thus depends on the ratio of these forces, which is characterized by the Weber number,

$$We = \left(\rho/\sigma_s\right)u^2 d \tag{6.6}$$

where ρ is the water density, σ_σ is the surface tension, u is the turbulent velocity fluctuation on the length scale of the bubble, and d is the bubble diameter. Within the Kolmogorov inertial sub-range, the fluctuation velocity relates to the dissipation rate of the turbulent kinetic energy as,

$$u \sim (\varepsilon d)^{2/3} \tag{6.7}$$

Turbulent bubble fragmentation is expected when the Weber number exceeds its critical value, We_{cr}. This condition corresponds to inequality $d > a_H$, where

$$a_H = We_{cr}^{3/5}\left(\sigma_s/\rho\right)^{3/5}\varepsilon^{-3/5} \tag{6.8}$$

is the *Hinze scale*, which is typically of the order of 1 mm. Hinze (1955) estimated the critical value of the Weber number as 0.2. More recent experiments by Lewis and Davidson (1982), Martinez-Bazan et al. (1999), and Deane and Stokes (2002) suggest that We_{cr} lies in the range from 3 to 4.7. Bubbles smaller than the Hinze scale are stabilized by surface tension, and the process of turbulent fragmentation is believed to be less important for these small bubbles.

Garrett et al. (2000) pointed out a major caveat for the turbulent fragmentation theory. Though the considerations leading to Eq. (6.5) are similar to those leading to Kolmogorov's inertial sub-range in the energy spectrum of isotropic turbulence, there is one significant difference. In the Kolmogorov cascade the energy ultimately cascades into eddies at the Kolmogorov scale $\eta_T = \left(\nu^3/\varepsilon\right)^{1/4}$ or less, and then dissipates into heat due to viscosity. In the case of bubbles, the input air fragments into smaller and smaller bubbles until surface tension halts the cascade at the Hinze scale. Air would thus tend to accumulate in a large spectral peak at the Hinze scale that would only slowly disappear since bubble dissolution is a relatively slow process. At the time of the Garrett (2000) publication, such a peak was not observed in either field or laboratory experiments.

Spectrum (6.5) is based on the assumption that the total air fraction is not large enough to have a feedback effect on the fragmentation process. At first glance, this assumption seems to be supported by the Deane and Stokes (2002) laboratory observation that "…the measured [bubble] separation velocity was always a factor of 5 or greater than the expected rise velocity of the bubble products, and the buoyancy effects were therefore assumed to be an unimportant source of bias." However, the Dean and Stokes experiment studied plunging breakers, which are not typical for open ocean conditions. In addition, the collective behavior of bubbles can result in significant fluctuations of the rising velocity of individual bubbles (Göz et al. 2001); the velocity fluctuations are mainly responsible for bubble fragmentation. The second mechanism, the rising-bubble fragmentation due to buoyancy forces, therefore cannot be completely discounted on the basis of the Deane and Stokes (2002) observation.

The spilling wave breaker resembles a turbulent bore (Sect. 1.6.4), which is an organized structure characterized by the regime of marginal stability in which the buoyancy and inertial forces are balanced in such a way that the Richardson number is close to its critical value (Turner 1973). The Kolmogorov cascade has to be replaced here with the concept of marginal stability in the bore-like wave breaker.

If we assume that the mechanism of bubble fragmentation due to buoyancy forces does dominate in spilling breakers and identify w_b as the determining parameter (replacing dissipation rate ε), then standard dimensional analysis leads to the following size spectrum:

$$N(r) \propto Q w_b^{-1} r^{-3} \tag{6.9}$$

An assumption that for large bubbles the rise velocity is approximately constant results in the -3 power law, which is close to the $-10/3$ power law in Eq. (6.5). Since bubble rise velocity w_b depends on the bubble radius r (Fig. 6.2), the power-law scaling in Eq. (6.9) can be different for different parts of the spectrum. Spectrum (6.9) should therefore be used with parameterization formulas (6.2) and (6.3).

Remarkably, Eq. (6.9) does not contain ε as a determining parameter. (From Chap. 3, the reader knows how difficult is to measure the dissipation rate in a breaking wave.)

Previously published distributions (Farmer et al. 1998; Bowyer 2001 and others) were unimodal. These averaged together many plumes of diverse types along with the background, thereby eliminating the multiple peaks. Leifer et al. (2003) and Leifer and de Leeuw (2006) developed a plume-type classification scheme. When analyzed separately, populations of different plume types (measured in a wind–wave tank) appeared to be multimodal. The wind–wave tank experiments, however, appear to produce the bubble size distributions that are quite different from those observed in the open ocean (Norris et al. 2013).

Figure 6.4 shows a comparison of bubble size spectra collected in the open ocean, surf zone, and laboratory tank. The laboratory data are neither representative of the surf zone nor of the open ocean. The bimodal distribution of spectra obtained from the laboratory experiment is not observed in any of the surf zone or open ocean

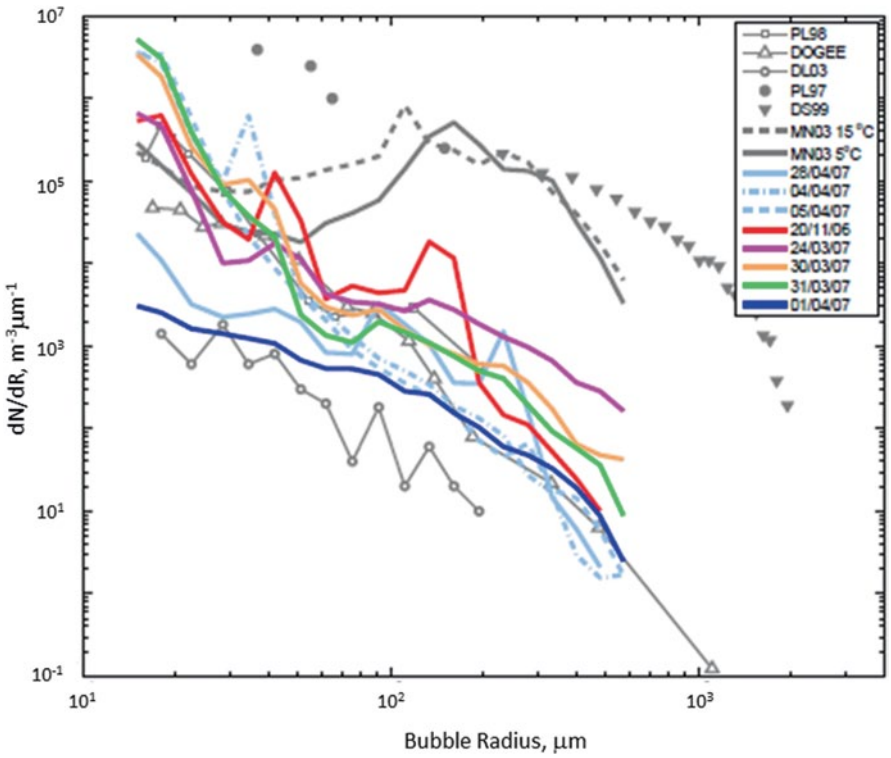

Fig. 6.4 Averaged bubble population distributions from the open ocean buoy deployments by Norris et al. (2013) (colored lines) in comparison with surf zone and laboratory measurements. The open ocean bubble size spectra of de Leeuw et al. (2003) (DL03, $U = 5.8$ m s^{-1}), Phelps and Leighton (1998) (PL98, depth 0.5 m, U, 12–14 m s^{-1}), Brooks et al. (2009), and Pascale et al. (2011) (DOGEE, averaged over a depth of 0–3 m, $U = 13$ m s^{-1}) and the surf zone spectra (filled symbols) of Phelps et al. (1997) and Deane and Stokes (1999) (DS99) along with the laboratory results of Mårtensson et al. (2003) at 5°C (solid gray line) and 15°C (dashed gray line) are also shown. Note that the Deane and Stokes (1999) data relate only to actively breaking surf regions. After Norris et al. (2013)

bubble spectra. The surf zone bubble size spectra appear to be two or three orders higher than the open ocean spectra.

The Norris et al. (2013) open ocean data were taken only 8 m from the ship hull, which might have distorted the wind–wave field with unknown consequences for the bubble spectrum. Their data, nevertheless, are close to the measurements of bubble spectra with a free drifting buoy by Pascal et al. (2011).

6.2.4 Bubble Dispersion and Diffusion

A bubble plume injected in the near-surface layer of the ocean during a wave-breaking event is subject to dispersion and turbulent diffusion. Larger bubbles rise to the

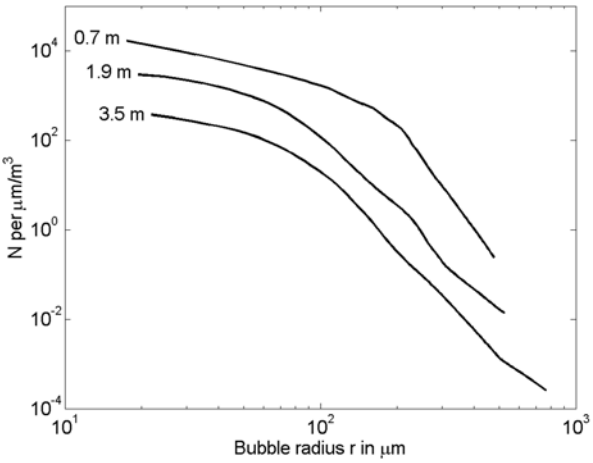

Fig. 6.5 The averaged bubble size spectrum at three depths below the surface, obtained at a wind speed of 11.9 m s^{-9}. After Garrett et al. (2000). Copyright © 2000 American Meteorological Society. Used with permission

surface within a few seconds, forming the whitecaps. Wave breaking also leaves numerous smaller bubbles that can persist for minutes.

Figure 6.5 shows averaged bubble size distributions acquired in the Gulf of Mexico by Farmer et al. (1998) and analyzed by Garrett et al. (2000) at depths 0.7 m, 1.9 m, and 3.5 m. The bubble density decreases with depth. The most significant drop for large bubbles ($r>200$ μm) is observed between 0.7 m and 1.9 m depths. A plausible explanation is that the 0.7 m depth is within the wave-stirred layer, while the observations at 1.9 m depth are outside this layer.

The spectra shown in Fig. 6.5 are averages over a sufficiently large time period (30 min). Since this time period included different types of wave-breaking events, possible bimodal spectral structures (like those shown in Fig. 6.4) could not be revealed.

Garrettson (1973) derived an equation governing the size distribution N of a cloud of bubbles at depth z. Thorpe (1982) simplified this equation by considering the cloud composed of small bubbles of a single gas (for instance, nitrogen) and of almost equal size. Ignoring acceleration and volume source terms (but retaining the dissolution term), and assuming horizontal isotropy transport Eq. (1.12) in application to bubbles takes the following form:

$$\frac{\partial C}{\partial t} = \frac{d}{dz}\left(K_B \frac{dC}{dz}\right) - w_b \frac{dC}{dz} - \sigma_* C \tag{6.10}$$

where C is the volume concentration of bubbles, w_b is the bubble rise speed, σ_* is the bubble dissolution rate, and K_B is the turbulent diffusion coefficient for bubbles.

The terms on the right side of Eq. (6.10) represent the downward turbulent diffusion of bubbles from the surface wave-breaking zone, the vertical rise of bubbles

toward the surface, and the dissolution and decay of bubbles, respectively. In the Thorpe (1982) model, an additional assumption is that the total number of bubbles decreases at the same rate as the radius decreases.

With a simplified parameterization for the turbulent mixing coefficient

$$K_B = \kappa u_* |z| \tag{6.11}$$

and the bubble decay rate

$$\sigma_* = \alpha z / (1 + |z| / H_0) \tag{6.12}$$

(here $H_0 = p_0 / g\rho \approx 10$ m, where p_0 is the atmospheric pressure), Thorpe (1982) obtained the following solution of (6.10):

$$N / N_0 = (\mu |z|)^{-\lambda/2} H_{\lambda/2}(\mu |z|^{1/2}) \tag{6.13}$$

where $H_{\lambda/2}$ is the modified Bessel function chosen so that $N \to 0$ as $z \to -\infty$, $\lambda = w_b / (\kappa u_*)$, $\mu = (\alpha / (\kappa u_*))^{1/2}$, and N_0 is a constant.

Since wave-breaking turbulence is not included in the mixing parameterization, there is a singularity of the air bubble flux at $z = 0$. In order to preserve the flux of bubbles, the value $\partial N / \partial z \to \infty$ was avoided by selecting the initial depth $z_0 = 0.5$ m and the maximum depth $z_{max} = 10$ m. This selection of initial depth away from the ocean surface also avoids discussion of the near-surface breaking wave zone where the assumed form of K_B is not valid. The solutions for bubbles with radius $a_0 = 50$ μm, $w_b = 0.54 \times 10^{-2}$ m s^{-1}, and $\alpha \approx 4 \times 10^{-3}$ s^{-1} m^{-1} were qualitatively consistent with the observations of Johnson and Cooke (1979). The assumptions about the mixing coefficient and choice of other parameter values were, however, tenuous and suspension of bubbles by the turbulent flow could not be included in the Thorpe (1982) pioneering work.

Recent developments in computational fluid dynamics methods have opened new opportunities for modeling of air bubble dynamics in the near-surface layer of the ocean. Liang et al. (2011) have developed a bubble concentration model and a dissolved gas concentration model for the oceanic boundary layer. The Liang et al. (2012) bubble model solves the extended version of Eq. (6.10) including a set of concentration equations for multiple gases in bubbles of different sizes; in addition, a dissolved gas concentration model simulates the evolution of dissolved gases and dissolved inorganic carbon. This sophisticated model based on the direct numerical simulation (DNS) method accounts for advection, diffusion, bubble buoyant rising, bubble size changes, gas exchange between bubbles and ambient water, and chemical reactions associated with the dissolution of CO_2. However, verification of numerical models with observational data is still a challenge.

In addition to dispersion and turbulent diffusion, small bubbles are drawn into the convergence zones produced by spatially coherent organized motions in the near-surface layer of the ocean (Chap. 5).

6.2.5 *Buoyancy Effects in Bubble Plumes*

The process of surface wave breaking and air entrainment have considerable dynamical coupling. A substantial part of the fluctuation energy during wave breaking may work against buoyancy forces (Woolf 1997).

Buoyancy effects in a two-phase environment can be understood from the classic budget equation for turbulence kinetic energy (TKE), similar to that in the theory for the flow with suspended particles developed by Barenblatt and Golitsyn (1974) for modeling dust storms. This theory predicts reduction of the turbulent drag coefficient in the suspension flow. Application of the Barenblatt and Golitsyn theory to the air bubble plumes produced by breaking waves, however, is not straightforward. In particular, the Kolmogorov number criteria (which is the analog of the Richardson number introduced for suspension flows) cannot be applied directly to the bubble-saturated upper ocean because the near-surface turbulence is produced by breaking waves rather than by mean horizontal shear (as in dust storms). The discussion in this section is therefore mainly qualitative rather than quantitative. Another aspect of this theory is that it does not explicitly include bubble size distribution. However, only relatively small bubbles can be entrained by the upper ocean turbulence and provide buoyant (negative) feedback on turbulence levels. Larger bubbles by themselves can induce turbulence in the near-surface layer of the ocean. Bubbles with radius exceeding approximately 1 mm shed unsteady vortices; the bubble trajectory also becomes unstable, changing from rectilinear to zigzag trajectories (Lima-Ochoterena and Zenit 2003). Generally, the bubble-induced water turbulence and the rise velocity of bubble swarms are different from those of single bubbles, due to bubble interactions (Göz et al. 2001).

The average void fraction of air due to bubbles from field measurements is given in Table 6.3 as a function of depth. In its contribution to the buoyancy, the maximum air fraction of 0.016% observed at 0.1 m depth is equivalent approximately to a 0.5°C change in water temperature. The average air fraction rapidly drops with depth (Table 6.3).

During an active phase, the bubble plume may contain a volume fraction of air that is much greater than the average over many wave periods. For comparison, the observations of Bowyer (2001) averaged over wave-breaking events gives the volume air fraction of as much as 0.12%, which is equivalent to a 3.75°C change in water temperature in terms of buoyancy.

The relatively high concentration of bubbles that is required for buoyancy effects to be important is primarily observed in wave breakers and convergence zones (e.g., due to Langmuir circulations). A high void fraction due to air bubbles is present in the transition layer between air and water under very high wind speed conditions (Sect. 6.4.3).

The vertical profiles of air-fraction obtained with bow sensors in the upper 2 m of the ocean under relatively strong winds are shown in Fig. 6.6. The idea of extracting this type of profile from bow sensors emerged during communication of one of the authors (Soloviev) with Kennan Melville from Scripps Institution of Oceanography.

Table 6.3 Average void fraction for the conditions of developed seas. The measurements are taken from wave-following buoys.

Source	Depth (m)	Void fraction (%)	Wind speed ($m\ s^{-1}$)	Wave height (m)	Fetch
Bowyer (2001)	0.1	0.016	10–12	2	Unlimited
Bowyer (2001)	0.6	0.0054	11–13	2.5	15–120 km
Farmer et al. (1998) and Garrett et al. (2000)	0.7	0.0060	12		>100 km
Farmer et al. (1998) and Garrett et al. (2000)	1.9	0.00030	12		>100 km
Farmer et al. (1998) and Garrett et al. (2000)	3.5	0.000044	12		>100 km

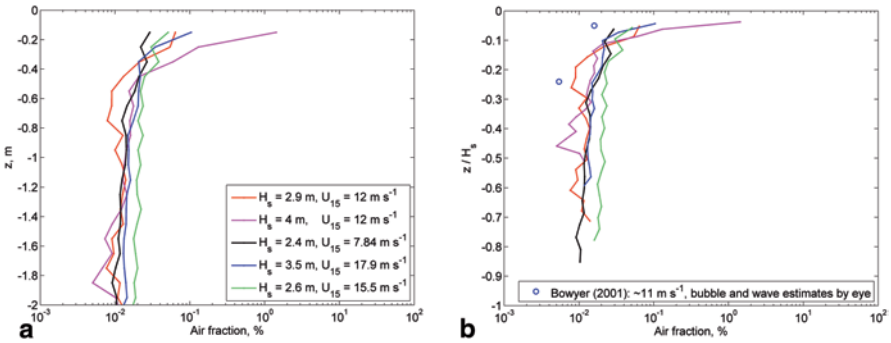

Fig. 6.6 **a** Average vertical air-fraction profiles in the near-surface layer of the ocean obtained by the authors of this monograph with the conductivity sensor installed on the bow of the vessel during the TOGA COARE experiment (more details in Sect. 3.3.5). The wind speed range is from 8 m s^{-1} to 15.5 m s^{-1}. Depth is calculated as distance from the "instantaneous" position of the sea surface. **b** Data from the bow sensor from the upper 1 m of the ocean normalized by significant wave height in comparison with the Bowyer (2001) data (shown as open circles).

The data shown in Fig. 6.6 suggest that the air concentration close to the sea surface can exceed 1 %. Note that in terms of contribution to buoyancy, a 1 % difference in water density is equivalent to a 30°C temperature difference.

Under moderate wind speeds, wave-breaking events last only about 1 s; the whitecap area associated with the wave breaker occupies a relatively small fraction of the sea surface. The whitecap coverage increases rapidly with wind speed. According to Monahan and O'Muircheartaigh (1980), the fractional coverage of the stage B whitecaps, which are the surface expression of decaying bubble plumes, is a strong function of wind speed:

$$W_c \approx 3.84 \times 10^{-4} U_{10}^{3.41} \tag{6.14}$$

where U_{10} is the wind speed at 10 m height. Bortkovskii ((1983) found that the whitecap coverage varies with temperature (though he offered no parameterization for its temperature dependence).

Equation (6.14) predicts that $W_c = 1$ at $U_{10} = 38.7$ m s^{-1}. Extrapolation of Eq. (6.14) to such high wind speed, of course, does not make sense. In fact, the Anguelova and Webster (2006) analysis shows that the whitecap coverage does not exceed 10% even in hurricane conditions. Nevertheless, sea state photographs taken during a hurricane (Fig. 6.1) show that above $U_{10} = 40$ m s^{-1}, the sea surface in fact becomes completely covered with the "whiteout" consisting of foam and streaks (Holthuijsen et al. 2012). This suggests that mechanisms other than whitecapping dominate production of the whiteout during hurricanes (see Sect. 6.4.3).

So far neither the bubble buoyancy effects on near-surface turbulence nor the bubble-induced turbulence has been investigated thoroughly in the open ocean.

6.3 Sea Spray Aerosol Production

6.3.1 Introduction

The ocean surface layer is a source of *sea spray* and *marine aerosols*. According to estimates given in Monin and Krasitskii (1985), about 0.3% of the world ocean surface is covered with breaking waves and the total salt flux into the atmosphere is about 10^{12} kg per year.

The sea spray is an important factor in the air–sea transfer of heat, moisture, and momentum under high wind speed conditions. The primary marine aerosol is composed of seawater enriched with chemical compounds, insoluble organic matter as well as living microorganisms (bacteria, viruses). Both natural and anthropogenic compounds, dissolved in the near-surface layer of the ocean or as a thin film on the ocean surface, contribute to the content of marine aerosols. Large spray drops return to the ocean before evaporating, so these compounds are also returned. Smaller drops are entrained into the turbulent air flow in the marine boundary layer and, under favorable conditions, completely evaporate producing sea-salt aerosol particles, which are effective cloud condensation nuclei. Influencing the development and albedo of clouds, sea-salt aerosols can influence climate.

Sea-salt particles are an important part of the atmospheric sulfur cycle (Chamides and Stelson 1992). According to O'Dowd et al. (1999), natural and anthropogenic sulfate aerosols influence the climate. The Intergovernmental Panel on Climate Change (2001) estimated the direct and indirect radiative forcing of sulfate aerosols to be in the range –0.2 to –0.8 W m^{-2} and 0 to –1.5 W m^{-2}, respectively. This is comparable in magnitude to the radiative forcing of anthropogenic greenhouse gases. It is important that sulfate aerosols produce a radiative effect that is opposite in sign to that of anthropogenic greenhouse gases.

In addition to affecting climate, marine spray and aerosols transfer pollutants from the ocean to the atmosphere, serve as a tracer in the climate record of Arctic and Antarctic snow and ice cores, play a role in corrosion, and cause vegetation stress in coastal regions. The optical properties of the marine boundary layer depend substantially on the type and concentration of aerosols.

Note here that some studies cited below, like that of Andreas (1998), use the diameter of wet particles (i.e., of droplets), while others, like that of Mårtensson et al. (2003), use the diameters of dry particles. This can be attributed to different applications of marine aerosol results. Air–sea interaction scientists are interested in the influence of marine aerosols on the air–sea fluxes, while climatologists are mostly concerned with the presence of dry aerosol particles in the atmosphere. Respectively, different definitions for the sea spray and aerosol generation functions can be found in the literature. In particular, A convention of specifying the size of sea spray particles and dry aerosol particles can be found in de Leeuw et al. (2011).

6.3.2 Mechanisms of Sea Spray Production

There are basically three varieties of spray droplets: film droplets, jet droplets, and spume droplets. We first consider film and jet droplets.

Bursting air bubbles create film and jet droplets. Bubbles are primarily generated through entrainment by breaking waves (Thorpe 1986). After being carried to some depth by a plunging wave jet, a bubble then rises to the surface where it bursts. The process of bursting is schematically illustrated in Fig. 6.7. As the bubble emerges from the water, a thin film forms at the upper surface of the bubble; the film thins by drainage and eventually ruptures. When the bubble film opens, the rim of the receding film cap ejects tens to hundreds of film droplets with radii ranging roughly from 0.5 to 5 μm (Spiel 1998). The collapsing bubble cavity shoots up a jet of water from its bottom. Due to velocity differences along this jet, it soon breaks up into a few jet droplets with radii typically ranging from 3 to 50 μm, depending on the size of the bubble that created them.

The number and size distribution of film and jet drops are connected to the bubble size distribution. Small bubbles produce only jet drops. The size of the jet drops is about 1/10 of the parent bubble diameter size; the bursting bubble produces a maximum of six jet droplets; bubbles larger than 3.4 mm produce no jet drops (Spiel 1997). Jet drops, hence, dominate in the super-micrometer aerosol range.

In addition to film and jet droplets, spume drops are produced by direct "tearing of water" from wave crests at wind speeds higher than about 9 m s^{-1} (Monahan et al. 1983). The spume drops are the largest spray droplets; minimum radii are generally about 20 μm and there is no definite maximum radius. Spume generation is associated with eliminating the clearly defined air–sea interface under high wind speed conditions. Koga (1981) and Veron et al. (2012) have shown from observations in a wind–wave tank that near the crest of the wave, where the wind stress is generally the highest, small projections develop, which then break up to form spume droplets.

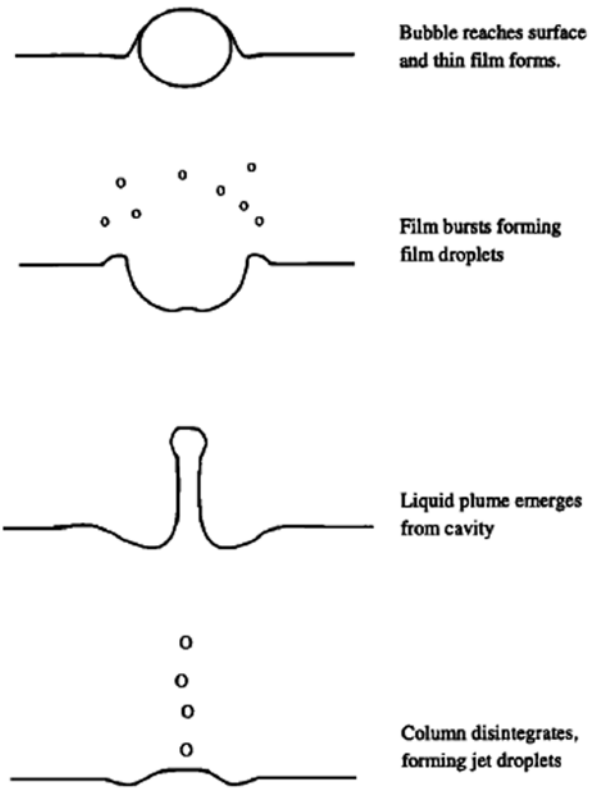

Fig. 6.7 Creation of droplets by bursting bubble at water surface. After Pattison and Belcher (1999). Reproduced by permission of American Geophysical Union

The maximum diameter of these droplets was about 3 mm. The projections presumably develop due to Kelvin–Helmholtz (KH) instability of the air–sea interface, which is discussed later in this chapter.

Droplets with radii in the range 10–500 μm contribute most to the heat fluxes at high wind speeds (Andreas 1992). This size range is dominated by spume droplets, implying that spume generation is the most important mechanism of droplet generation for mediating fluxes under very high wind speed conditions.

The terminal velocity of the largest drop that is stable in the gravitational field (assuming an oblate-spheroid shape of the droplet) scales according to Pruppacher and Klett (1978) as follows:

$$w_t \approx \left(\frac{4\pi b_a}{3aC_D}\right)^{1/2}\left(\frac{\rho g\sigma_s}{\rho_a^2}\right)^{1/4}, \tag{6.15}$$

where b_a is the axial ratio of the oblate spheroid ($b_a \approx 0.55$), C_D is the drag coefficient ($C_D \approx 0.85$), and σ_s is the surface tension at the air–sea interface. For air-temperature of 20 °C and normal atmospheric pressure of 101.3 kPa, the terminal velocity is equal to $w_t \approx 7.8$ m s^{-1}. Equation (6.15) is relevant for drops $r > 2$ mm.

The transport equation for a large droplet in an equilibrium thermodynamics state and in a statistically steady and horizontally homogeneous marine boundary layer is as follows (Iida et al. 1992):

$$w_t \frac{dC}{dz} + \frac{d}{dz}\left(K_D \frac{dC}{dz} \right) = 0. \tag{6.16}$$

A plausible parameterization for the turbulent diffusion coefficient in a coordinate system connected to the sea surface is

$$K_D = Sc_T^{-1} \kappa \left(z + z_{0a} \right) u_{*a}, \tag{6.17}$$

where Sc_T is the turbulent Schmidt number for water droplets (of the order of unity) and z_{0a} is the surface roughness parameter from the air-side of the air–sea interface, for instance, expressed via Charnock's (1955)-type parameterization,

$$z_{0a} = 0.0185 u_{*a}^2 / g. \tag{6.18}$$

The solution for Eqs. (6.16) and (6.17) for C are as follows:

$$C = C_0 \left(1 + z / z_{0a} \right)^{-w_t / \kappa u_{*a}}, \tag{6.19}$$

where C_0 is some reference concentration at $z = 0$.

At $u_{*a} = 2$ m s^{-1} (corresponding to $U_{10} \approx 40$ m s^{-1}), the terminal velocity for the largest spray droplets $w_t \approx 8$ m s^{-1}: $w_t / \left(\kappa u_{*a} \right) \approx 10$. From Eq. (6.19), it follows that the droplet concentration should decrease at $z = z_{0a}$ by a factor $2^{10} \approx 10^3$ relative to the reference concentration, C_0. The surface roughness length scale, z_{0a}, following from the Charnock (1955) parameterization is of the order of 1 cm. As a result, in a purely diffusive model, the concentration of the largest droplets should drop dramatically with distance from the sea surface.

Though the turbulent diffusion mechanism apparently is not effective for the largest droplets, these droplets after tearing from the wave crest are taken up by the wind and typically fly some distance in the horizontal direction before reentering the ocean surface.

6.3.3 Sea Spray Source Function

The sea spray source or generation function, defined as the rate at which spray droplets of any given size are produced at the sea surface, is essential for many applications. The sea spray generation function, commonly denoted as dF_0 / dr_0 (e.g.,

Monahan et al. 1986), where F_0 is total droplet flux from the ocean and r_0 is the radius of a droplet at its formation, has units of number of droplets produced per square meter of surface per second per micrometer increment in droplet radius. For the consideration of spray momentum, heat, and moisture transfer, the generation function expressed as a volume flux, $\left(4\pi r_0^3/3\right)dF_o/dr_0$, is more suitable.

Andreas (1998) compared the results of different authors only to find that the existing parameterizations of the primary marine aerosol source differ by 6–10 orders of magnitude (Fig. 6.8). He nevertheless found some consistency in the estimated shape of the spray generation function. The volume flux is relatively small for droplets with radii less than 2 μm or exceeding 500 μm; there is a 2–3 order-of-magnitude peak in the spray generation function between approximately 10 μm and 200 μm. This peak appears in the spume droplet region, which contributes most to the heat and momentum fluxes at high wind speeds. Parameterization of spume droplet production is therefore essential for evaluating the effects of spray on air–sea heat and moisture transfer.

The estimated generation rates differ so greatly mainly due to the use of different sets of droplet concentration data and differences in the assumptions made regarding droplet trajectories. The process of droplet evaporation also adds to the uncertainty. Ultimately, Andreas (1998) discounts some of the parameterizations shown in Fig. 6.8 based on different grounds and ultimately focuses his analysis on the results of Smith et al. (1993) and Monahan et al. (1986) to produce the following parameterization:

$$\frac{dF_{MS}}{dr_0} = 3.5\frac{dr_{80}}{dr_0}\frac{dF_s}{dr_{80}},$$

$$\text{where } \frac{dF_s}{dr_{80}} = \begin{cases} C_1\left(U_{10}\right)r_{80}^{-1}, & 10 \le r_{80} \le 37.5\ \mu\text{m} \\ C_2\left(U_{10}\right)r_{80}^{-2.8}, & 37.5 \le r_{80} \le 100\ \mu\text{m} \\ C_3\left(U_{10}\right)r_{80}^{-8}, & 100 \le r_{80} \le 250\ \mu\text{m} \end{cases} \tag{6.20}$$

in which the spume extrapolation (third line) is based on droplet concentration data obtained within 0.2 m of the surface by Wu (1984). Here C_1, C_2, and C_3 are the wind-speed dependent coefficients ($\sim U_{10}^3$) that are evaluated by matching wind-dependent coefficient C_1 to the Smith et al. (1993) parameterization at $r_{80} = 10\ \mu\text{m}$, where r_{80} is the radius of spray droplets in equilibrium at a relative humidity of 80 %. Coefficient C_2 is determined from the continuity condition at $r_{80} = 37.5\ \mu\text{m}$. Coefficient C_3 is then similarly found at $r_{80} = 100\ \mu\text{m}$. The relationship between r_{80} and r_0 (the radius of a droplet at its formation) is as follows:

$$r_{80} = 0.518 r_0^{0.976} \tag{6.21}$$

The parameterizations that are currently in use for various applications are still with a few orders of magnitude differences (Andreas et al. 2010; de Leeuw et al. 2011). Furthermore, the existing data do not cover hurricane wind conditions (U_{10}>30–40 m s^{-1}). As a result, the sea spray generation function for hurricane conditions

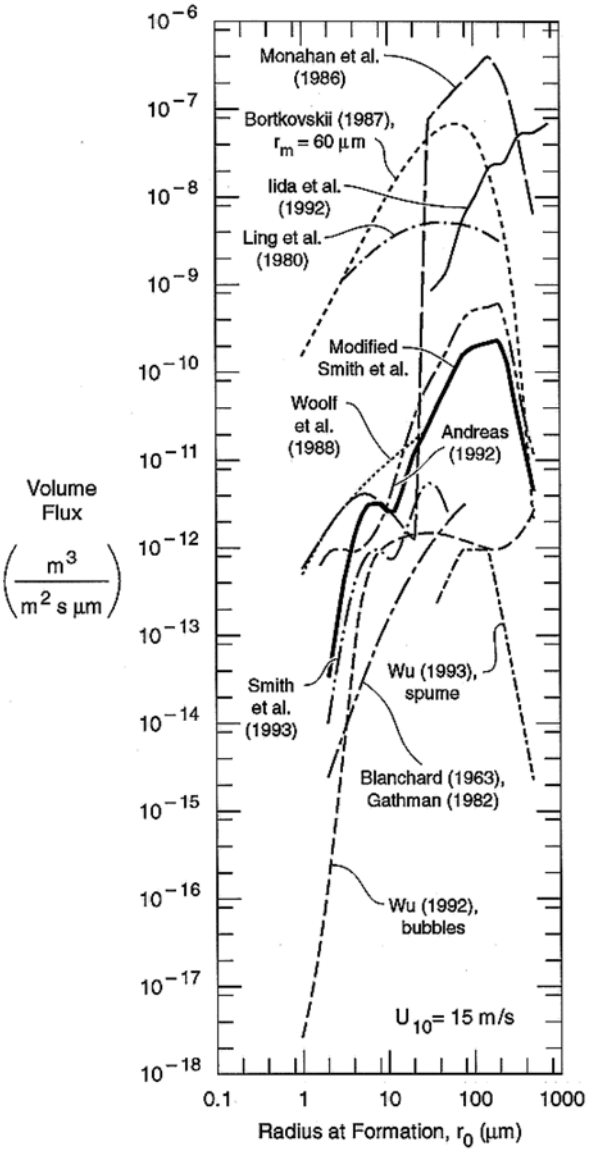

Fig. 6.8 Various estimates of the sea spray generation function expressed as the volume flux, $\left(4\pi r_0^3/3\right)dF/dr_0$, for U_{10} of 15 m s^{-1}. After Andreas (1998). Copyright © 1998 American Meteorological Society. Used with permission

remains practically unknown. Andreas (1998) has concluded that there is no trustworthy spray generation function even for a wind speed exceeding 20 m s^{-1}. Extrapolation of parameterization to hurricane conditions undertaken by some authors is not based on any data.

The dynamics of large droplets is a critical issue in developing the spray generation function for high wind speed conditions. After the initial ejection or splashing from the wave crest region these droplets fall quickly and do not diffuse to any significant height above the ocean, though can be taken up by the wind gust and fly some distance in the horizontal direction before reentering the ocean surface (Koga 1981; Veron et al. 2012). The largest droplets may therefore have eluded complete characterization during previous field experiments.

6.3.4 Primary Aerosol Number Distributions

Marine aerosol production is a major contributor to global natural aerosol systems (Lewis and Schwartz 2004; O'Dowd and Leeuw 2007; Clarke et al. 2006; de Leeuw 2011). The Earth's radiative budget, biogeochemical cycling, visibility, remote sensing, impacts on ecosystems, and regional air quality significantly depend on the contribution from marine aerosol. Marine aerosols include primary components, which are a result of air–sea interactions, and secondary components, which result from gas-to-particle conversion process. We consider here the mechanisms of the primary marine aerosol production. Reviews of the secondary aerosol production can be found in Lewis and Schwartz (2004) and O'Dowd and Leeuw (2007).

The size distribution function of bubbles in the upper ocean, which are the primary source of marine aerosols, depends on wave-breaking parameters, on temperature, salinity, and presence of surfactants. The primary marine aerosol generation is expected to depend on these parameters as well. Figures 6.9 and 6.10 show results of a laboratory experiment for quantifying the salinity and temperature dependence of primary marine aerosol generation.

Figure 6.9 illustrates the effect of salinity on the dry aerosol number concentration (N_p). For the interpretation of this graph recall that for a similar drop size spectrum at formation, the less saline droplets produced at the lower salinity will evaporate to particles with smaller dry particle diameter D_p. The ratio between the diameters of dry particles resulting from 33.0 and 9.2‰ salinity following from simple considerations is determined as $(33.0/9.2)^{1/3} \sim 1.5$.

For aerosols generated by bubbles in the saltwater solutions ($S_w = 9.2$‰ and 33.0‰), two modes are observed depending on the particle size (Fig. 6.9). For the higher salinity, the small particle mode appears as a peak at ~0.1 μm D_p, whereas for the lower S_w, the small particle mode appears as a peak that is roughly a factor 1.5 smaller. This is consistent with the above ratio estimate for the dry particle diameters evaporated from the same size wet particle but with different sea-salt concentration. For particles from the $D_p < 0.2$ μm range, the total volume varies approximately proportionally to the water salinity.

On the other hand, for $D_p > 0.2$ μm (with a peak at ~2 μm), the aerosol spectra have a similar shape for both salinities; the concentrations, however, are an order of magnitude different. This leads to the conclusion that for $D_p < 0.2$ μm, salinity does not affect the original droplet production, just the size of the residual dry aerosol.

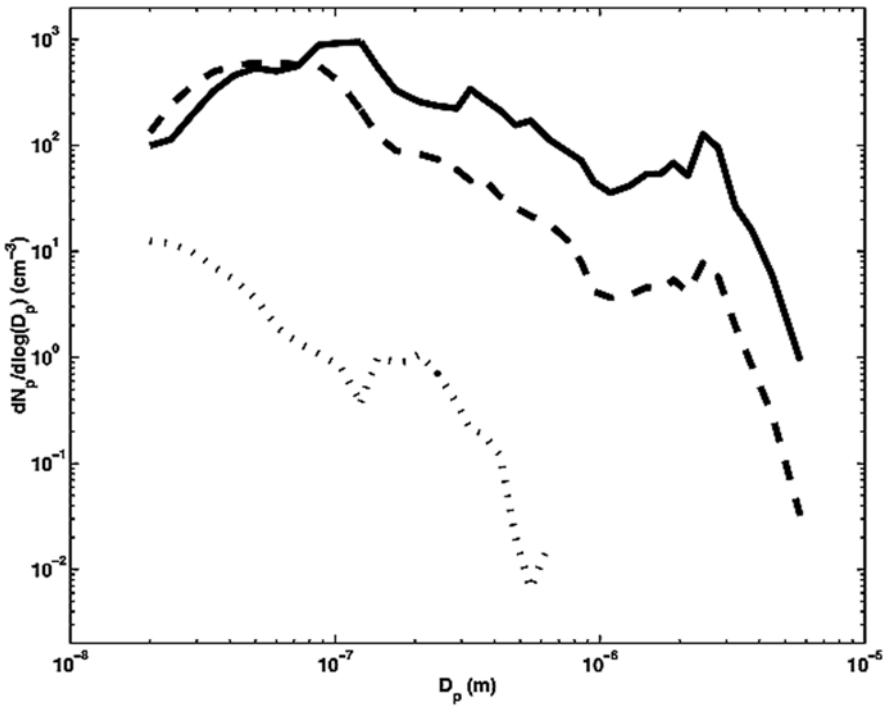

Fig. 6.9 Number distributions of primary aerosols produced from bubbles in water with salinity of 0.0‰ (dotted line), 9.2‰ (dashed line), and 33.0‰ (solid line) in a laboratory experiment. Water temperature was 23 °C. After Mårtensson et al. (2003). Reproduced by permission of American Geophysical Union

Note that at formation, droplets are assumed to have the salinity of the seawater (Andreas 1998). Figure 6.9 thus indicates different droplet formation processes for particles with D_p smaller than ~0.2 μm and for particles larger than this size.

Aerosol number size distributions for four water temperatures are presented in Fig. 6.10. For $D_p > 0.35$ μm, the number concentration increases with increasing temperature, and the shapes of the size distributions are similar at all temperatures. For $D_p < 0.07$ μm, the number concentration decreased with increasing temperature. The curves cross in a transitional range $0.07 < D_p < 0.35$ μm; however no clear trend with water temperature has been revealed for this transition. Similar to the salinity dependence (Fig. 6.9), the temperature dependence in Fig. 6.10 indicates different droplet formation processes, in this case below and above 0.07–0.35 μm D_p.

6.3.5 *Parameterization of Sea Spray Aerosol Production Flux*

De Leeuw et al. (2011) have analyzed different parameterizations for the production flux of sea-salt aerosol particles based on laboratory experiments and field

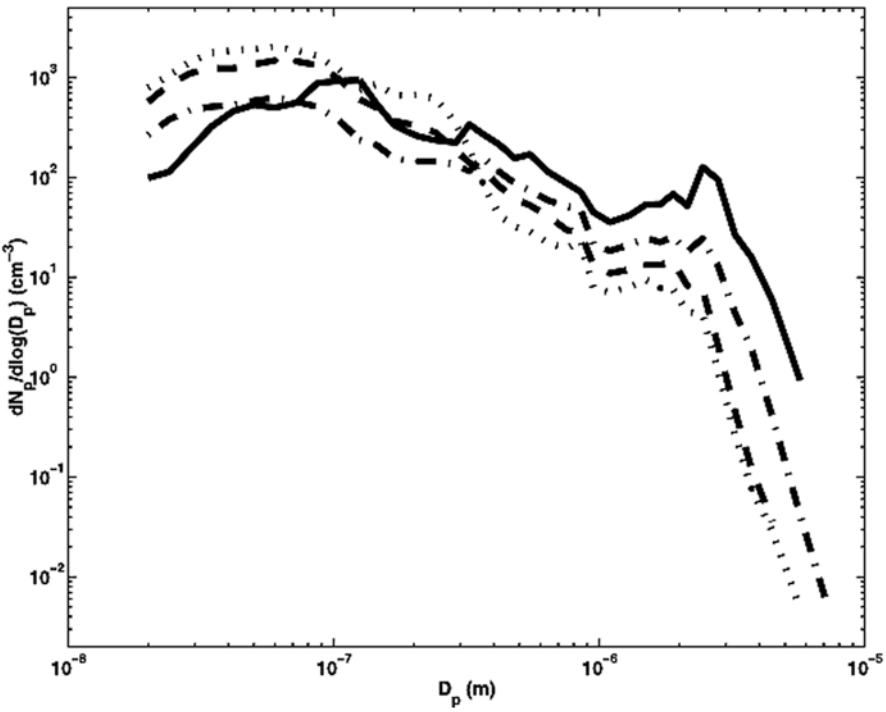

Fig. 6.10 Number distributions of primary aerosol produced at water temperatures of –2 °C (dotted line), 5 °C (dashed line), 15 °C (dot-dashed line), and 23 °C (solid line) in laboratory conditions. The salinity was 33‰. After Mårtensson et al. (2003). Reproduced by permission of American Geophysical Union

measurements, in the surf zone and in the open ocean (Fig. 6.11). The surf zone and laboratory results, however, are not representative of open ocean whitecapping processes, bubble size spectra, and sea spray aerosol flux. In fact, the wave-breaking turbulence and bubble plume dynamics in the open ocean are quite different from those in the surf zone and laboratory facilities (Norris et al. 2013).

For small particle sizes, contributions of organic matter to sea spray aerosol in areas with high biological productivity are important and may dominate for particle sizes $r_{80} < 0.25$ µm (Lewis and Schwartz 2004). Notably, this may also be applicable to hydrocarbon dispersion in the form of aerosol particles from oil spills into the atmosphere under strong winds and breaking waves.

Order-of-magnitude variation remains in estimates of the size-dependent production flux per whitecap area, the quantity central to formulations of the production flux based on the whitecap method. This uncertainty indicates that the production flux may depend on quantities such as the volume flux of air bubbles to the surface that are not accounted for in current models. Variation in estimates of the whitecap fraction as a function of wind speed contributes additional, comparable uncertainty to production flux estimates (de Leeuw et al. 2011; Holthuijsen et al. 2012).

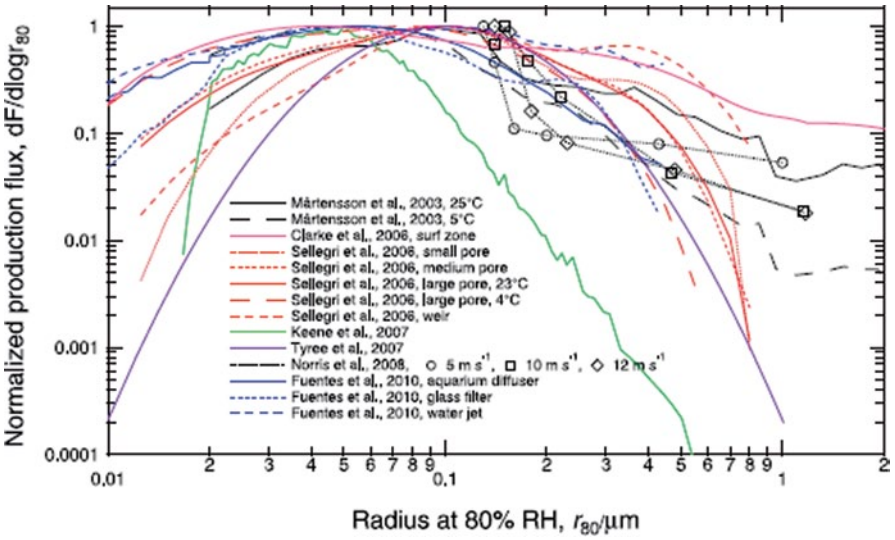

Fig. 6.11 Parameterization of sea spray aerosol production flux (normalized to maximum of size distribution) from the laboratory and field experiments discussed in de Leeuw et al. (2011) Copyright © 1999-2013 John Wiley & Sons, Inc.

Despite significant advances, the uncertainty in the sea spray aerosol production function remains very large. As a consequence, there is an almost two orders of magnitude spread in current estimates of global annual sea spray aerosol emissions (de Leeuw et al. 2011). The present knowledge of the aerosol production function limits the representation of emissions of sea spray aerosols in pollution transport models (e.g., for oil spill dispersion) or advanced climate models.

6.4 Air–sea Exchange During High Wind Speeds

6.4.1 Effect of Spray on Air–Sea Exchanges

Spray droplets that eventually become the main component of the marine aerosol are typically smaller than those that most influence air–sea heat and moisture transfer. Spume droplets, which are relatively large, are particularly important for the fluxes carried by sea spray. Andreas (1998) and Andreas and Emanuel (2001) estimated the effects of the sea spray on heat, moisture, and momentum transfer using a sea spray generation function that was extended into the range of spume droplet sizes. These authors employed a sea spray generation function valid in the droplet radius range from 2 µm to 500 µm based on the Andreas (1992) and modified Smith et al. (1993) parameterizations.

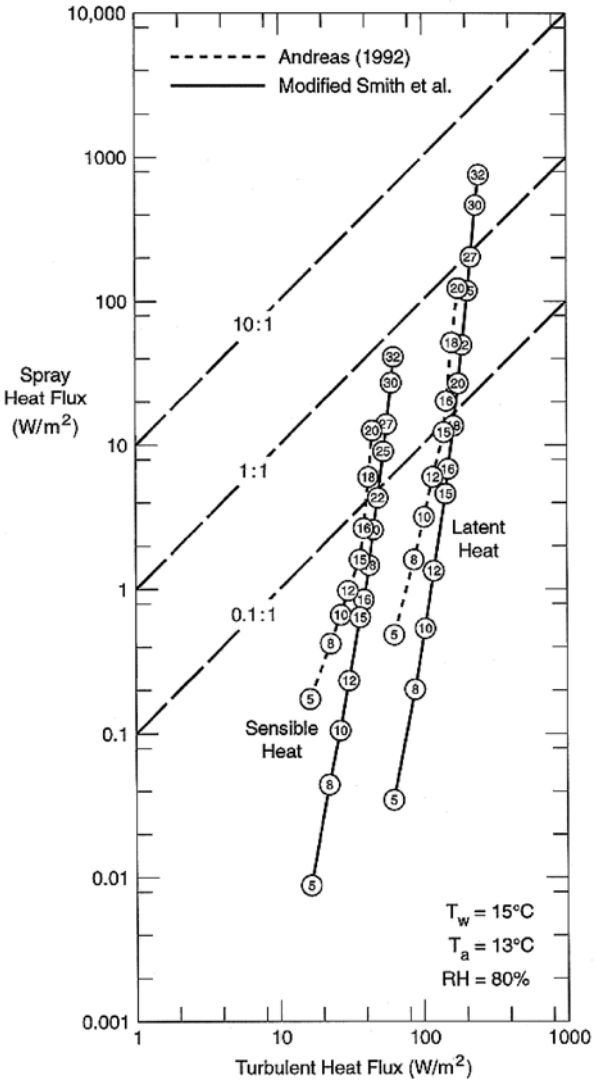

Fig. 6.12 Estimates of the sensible and latent heat fluxes from the Andreas (1992) spray model and two formulations for the spray generation function. The turbulent heat fluxes are estimated from bulk aerodynamic formulas. The surface water temperature (which is the initial temperature of the spray droplets) is T_w, the air temperature is T_a, and the relative humidity is RH. The number in each circle is the 10 m wind speed in m s^{-1}. The *diagonal lines* indicate where the spray and turbulent fluxes are equal (1:1), where the spray flux is 10% of the turbulent flux (0.1:1), and where the spray flux is 10 times the turbulent flux (10:1). After Andreas (1998). Copyright © 1998 American Meteorological Society. Used with permission

Figure 6.12 shows estimates of the magnitude of the sensible and latent heat fluxes based on the Andreas (1992) spray model and two formulations for the spray generation function—the one developed in Andreas (1992) and the modified param-

eterization of Smith et al. (1993). Differences between these generation functions are observed only for $U_{10} < 15$–16 m s^{-1}, when the contributions of sea spray to air–sea fluxes of heat and moisture are small. Figure 6.12 suggests the possibility of extremely large contributions of sea spray to heat and moisture transfer during storms.

Sea spray represents a volume source of heat and moisture in the marine boundary layer. The temperature and humidity profiles can be so strongly modified near the surface by the effects of evaporating spray that additional feedbacks may occur (Katsaros and de Leeuw 1994). The contribution of this feedback is still largely unknown due to the lack of reliable field data under very high wind speed conditions. Andreas' (1998) estimate does not include this feedback, though Fairall et al. (1994) have made an attempt to quantify the resulting sensible and latent heat flux above the droplet evaporation layer.

An important feature of the spray thermodynamics is that the processes of heat and mass exchange of a spray droplet with the air are decoupled. Figure 6.13 demonstrates this for a 100-μm radius spray droplet ejected into typical tropical cyclone conditions. The initial droplet temperature equal to the sea surface temperature drops from 28°C to its equilibrium temperature within 1 s, while only 1 % of the droplet mass must evaporate for the droplet to reach this equilibrium temperature (Andreas and Emanuel 2001). Remarkably little evaporation occurs until at least 40–50 s after droplet formation.

After spray is ejected into the atmosphere, wind can accelerate it. The time required for sea spray droplets starting with no horizontal speed to accelerate to within e^{-1} of the nominal wind speed U_{10} is shown in Fig. 6.14. This exchange extracts momentum from the flow, which is transferred to the ocean when spray droplets land back in the water (Andreas and Emanuel 2001). In surface-level winds of 10 m s^{-1} and higher, droplets with radii up to 500 μm reach a speed equal to the local speed within 1 s. An estimate of droplet residence time for all droplets up to 500 μm in radius suggests that this time is sufficient to accelerate to the local wind speed.

Thus, spray droplets with relatively short atmospheric residence time (the reentrant spray) effectively transfer momentum flux and sensible but not latent heat flux. Note that the latent heat flux is usually much larger than the sensible heat flux.

The spray momentum τ_{sp} and buoyancy B_{sp} vertical fluxes are defined from the following formulas (Andreas and Emanuel 2001):

$$\tau_{sp} = \frac{4\pi}{3}\rho_w U \int_{r_{lo}}^{r_{hi}} r_0^3 \frac{dF_0}{dr_0} dr_0, \tag{6.22}$$

where dF_0/dr_0 is the sea spray generation function and U is the wind speed at one significant wave height above the mean sea level. Equation (6.22) implies that all droplets reach this level. Some justification for this assumption comes from the fact that the droplets that contribute most to the spray momentum flux are the large ones torn right off the wave crests.

Equation (6.22) is nevertheless only an upper bound on the surface stress and vertical buoyancy flux that falling spray droplets produce on the ocean surface layer. In fact, some small spray droplets are entrained in the turbulent flow and never

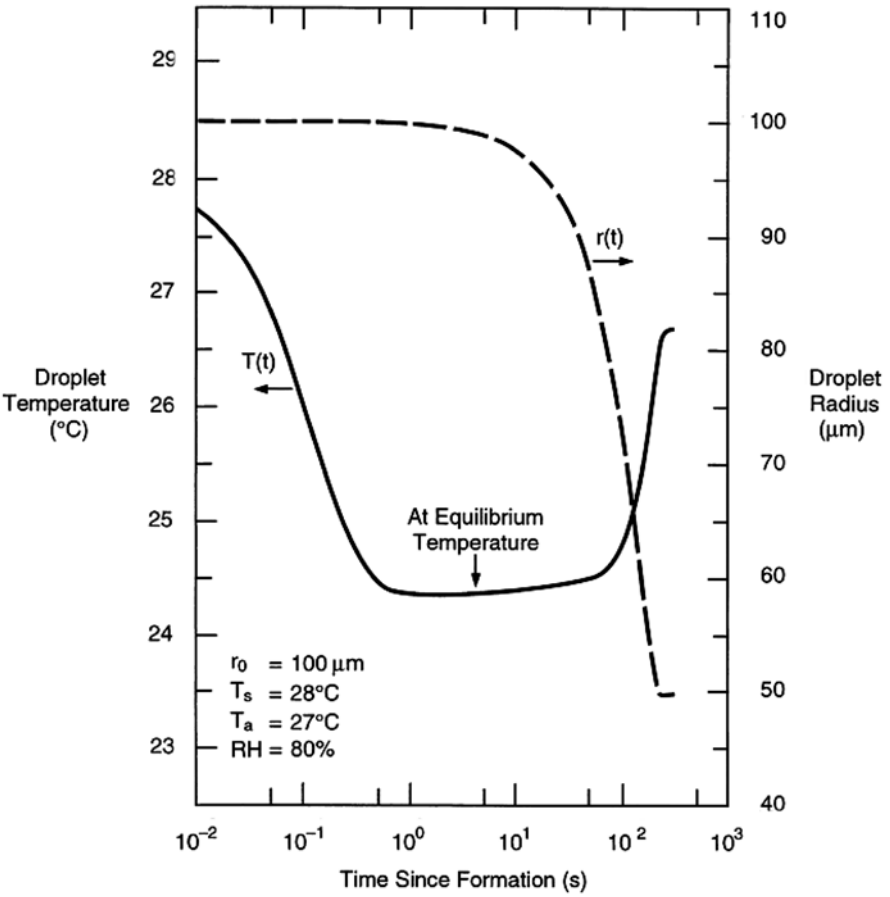

Fig. 6.13 Evolution of temperature and radius of a spray droplet of initial radius $r_0 = 100\ \mu$m, which is ejected from the sea surface at temperature $T_s = 28\,°$C into the air at temperature $T_a = 27\,°$C and relative humidity 80 %. The droplet has initial salinity 34 psu, and the barometric pressure is 1,000 mb. After Andreas and Emanuel (2001). Copyright © 2001 American Meteorological Society. Used with permission

return back to the ocean. The droplets that return to the sea partially evaporate and therefore have a reduced radius r_0, and thus reduced momentum.

Figure 6.15 shows the results of the estimation of τ_{sp} from Eq. (6.22) for two versions of the sea spray generation function in comparison with the total surface stress,

$$\tau = \rho_a u_{*a}^2, \tag{6.23}$$

where ρ_a is the air density and u_{*a} is the friction velocity in the air. The sea spray generation function has not yet been determined for friction velocities $u_{*a} \geq 2$

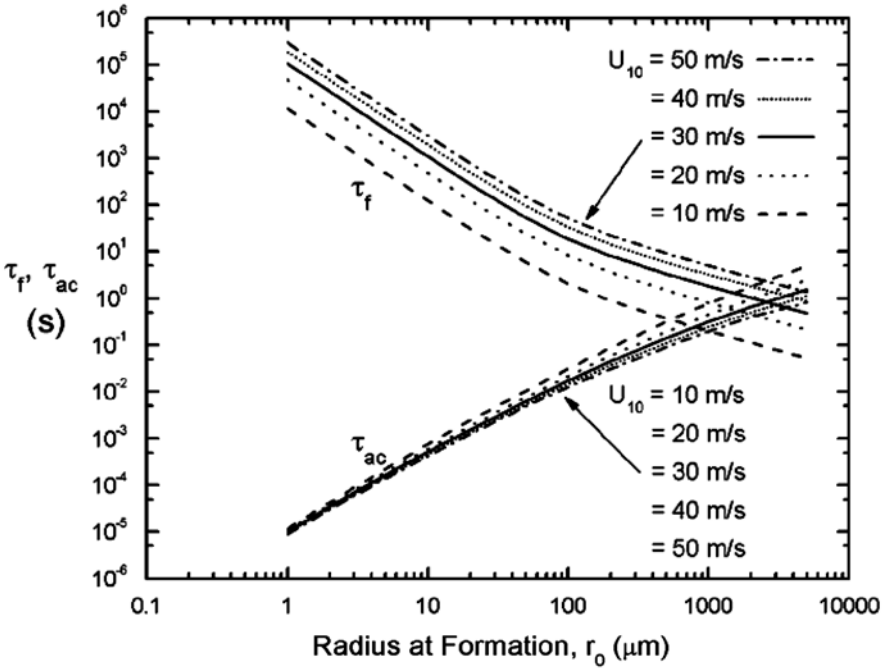

Fig. 6.14 Time τ_{ac} required for sea spray droplets to accelerate to wind speed U_{10}. Here, τ_f is the typical atmospheric residence time for droplets of initial radius r_0 at the indicated wind speed calculated from relation $\tau_f = A_{1/3}/w_t$, where $A_{1/3}$ is the significant wave amplitude determined as $A_{1/3} = 0.015U_{10}^2$ ($A_{1/3}$ is in m and U_{10} is in m s^{-1}). The air temperature is taken as 20 °C, and the barometric pressure as 1,000 hPa. After Andreas (2004). Copyright © 2004 American Meteorological Society. Used with permission

m s^{-1}. In the range $u_{*a} < 2$ m s^{-1}, τ_{sp} estimated with (6.22) is much less than τ. Nevertheless, the estimated spray stress increases approximately as the fourth power of u_{*a}, because $dF_0/dr_0 \sim u_{*a}{}^3$ and U is approximately linear in u_{*a}. At the same time, τ is just quadratic in u_{*a}. Andreas (2004) therefore assumes that when the winds reach hurricane strength, spray stresses may become comparable to the total stress. Andreas and Emanuel (2001) proposed the following parameterization for the spray stress,

$$\tau_{sp} = 6.2 \times 10^{-2} u_{*a}^4, \tag{6.24}$$

which gives τ_{sp} in N m^{-2}, when u_{*a} is in m s^{-1}. They call parameterization (6.24) "heuristic" because it is based on their intuition rather than on any data. According to Fig. 6.15, the sea spray stress becomes comparable to the interfacial wind stress at about 60 m s^{-1} wind speed, which is consistent with Soloviev and Lukas (2010). Note that the sea spray contribution to the sensible and latent heat fluxes becomes comparable to the corresponding interfacial fluxes at about 30 m s^{-1} wind speed.

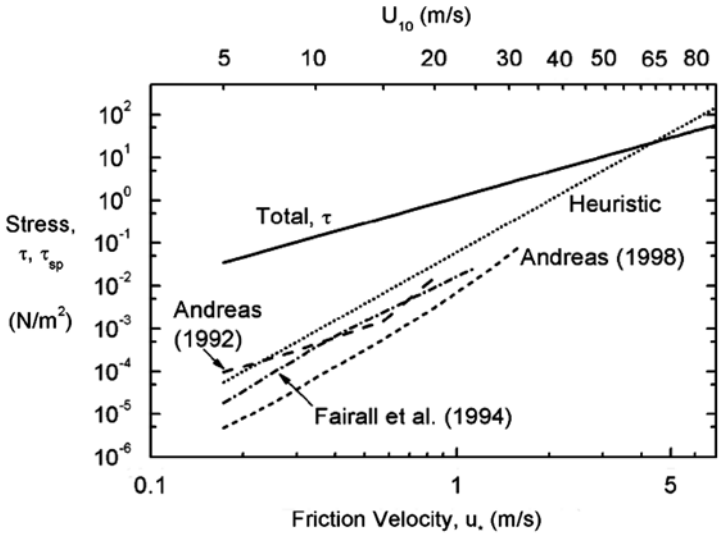

Fig. 6.15 Estimates of the total and sea spray stresses. The sea spray stresses are calculated from Eq. (6.22) for three versions of the sea spray generation function. The extent of these curves reflects the wind speed range over which the functions are appropriate. The total stress line is Eq. (6.23); the heuristic line is equation (6.24). After Andreas (2004). Copyright © 2004 American Meteorological Society. Used with permission

6.4.2 Dynamics of Suspension Flow

The spray-saturated atmospheric boundary layer can be represented as a suspension flow. The Barenblatt and Golitsyn (1974) theory for the flow with suspended particles in a dust storm can provide a theoretical basis for the analysis of the sea spray effects on the marine boundary layer. In this conceptual theory, a stationary turbulent flow of a dust–gas suspension is considered in the semi-infinite region $z \geq 0$ bounded from below by the horizontal plane $z = 0$. The suspension is a two-phase medium consisting of a gas with small particles; the concentration, volume, and weight of particles are small. The horizontal velocity components for the particles and gas are the same while the vertical components differ by the constant value a, which is the fall velocity of a single particle in unbounded space. Contributions due to particle interactions with the pressure and viscous stress are neglected due to the smallness of the particle concentration. Only density variations connected to the action of gravity are taken into account, which is the Boussinesq approximation. Under the Boussinesq approximation, the direct contribution of the solid phase to the momentum and momentum flux of the suspension are neglected. The analogy is of course not complete because in contrast to dust particles, sea spray experiences phase transformation (evaporation).

The laws of momentum and mass conservation for the suspension (Fig. 6.16) are as follows:

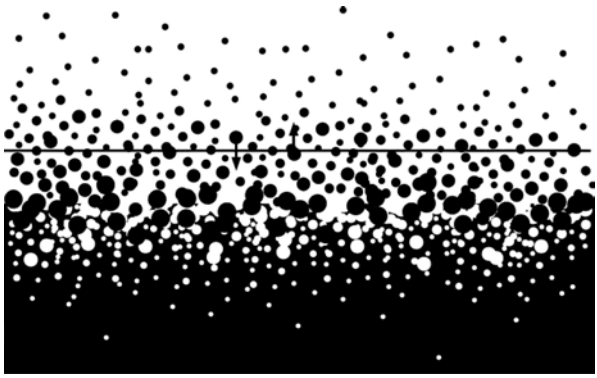

Fig. 6.16 Momentum and enthalpy transfer through an emulsion. Spray droplets are ejected upward and accelerate toward the free stream velocity, absorbing momentum from the atmosphere. After Emanuel (2003). Copyright © 2003 American Meteorological Society. Used with permission

$$-\rho\overline{u'w'} = \tau = \rho u_*^2 = const, \tag{6.25}$$

$$\overline{C'w'} = aC, \tag{6.26}$$

where C is the volume concentration of particles ($C = 4\pi r^3 n/3$), for which r is the particle radius, and n is the number of particles in the unit volume. Equation (6.26) reflects the fact that the vertical turbulent flux of the admixture is equal to its gravitational fallout.

The density of suspension is defined through its components:

$$\rho = \rho_g (1 - C) + \rho_p C \tag{6.27}$$

where ρ_g is the gas density and ρ_p is the particle density. The velocity vector $\vec{u}$ that consists of the longitudinal u and the vertical w components is defined in the following way:

$$\vec{u} = \left[\rho_g (1 - C)\vec{u}_g + \rho_p C\vec{u}_p\right] / \rho \tag{6.28}$$

where $\vec{u}_g$ and $\vec{u}_p$ are the gas and particle velocity vectors, respectively. For small volume ($C \ll 1$) and weight ($\sigma C \ll 1$) concentrations, the density fluctuations are:

$$\rho' = \sigma\rho C, \tag{6.29}$$

where

$$\sigma = (\rho_p - \rho_g) / \rho_g, \tag{6.30}$$

For water drops in the air $\sigma = (\rho - \rho_a) / \rho_a \approx \rho / \rho_a$.

The equation for the turbulent energy balance of the admixture is as follows:

$$\overline{\rho u, w,} du/dz + \overline{\rho' w'} g + \varepsilon = 0, \tag{6.31}$$

where ε is the dissipation rate of the turbulent kinetic energy. With Eq. (6.29), this equation can be presented in the form:

$$\overline{\rho u' w'} du/dz + \sigma \rho \overline{C' w'} g + \rho \varepsilon = 0 \tag{6.32}$$

The physical meaning of this equation is that the energy of turbulence generated by the mean shear flow is then spent partially for suspension and partially for dissipation. Introducing the nondimensional parameter,

$$K_t = \frac{g\overline{C' w'} \rho / \rho_a}{\overline{u' w'} du/dz} \tag{6.33}$$

which is known as the *Kolmogorov number*, Eq. (6.32) can then be presented in the following form:

$$\overline{u' w'} (du/dz)(1 - K_t) + \varepsilon = 0 \tag{6.34}$$

The solution of the problem appears to depend on a nondimensional parameter already familiar to us from Sect. 6.3.2:

$$\omega = w_t / (\kappa u_{*a}), \tag{6.35}$$

where w_t is the terminal velocity of the particle. For $\omega \geq 1$, the vertical distributions of the horizontal velocity u and concentration C are determined by the classical laws for the logarithmic boundary layer (Prandtl 1949):

$$u(z) = \frac{u_{*a}}{\kappa} \ln z + const_1, \quad C(z) = \frac{const_2}{z^{\omega}}, \tag{6.36}$$

which means that the particles do not affect flow dynamics.

For $\omega < 1$, the saturation-limited flow regime is possible, which is described by the following relation for the velocity and concentration profiles (Barenblatt and Golitsyn 1974):

$$u(z) = \frac{u_{*a}}{\kappa \omega} \ln z + const, \quad C(z) = \frac{a^2 K_t}{\sigma g z}, \tag{6.37}$$

For $\omega > 1$, the vertical mixing coefficient is defined as $K_m = \kappa u_{*a} z$, while for $\omega < 1$, it is given by equation

$$K_m = \omega \kappa u_{*a} z = w_t z, \tag{6.38}$$

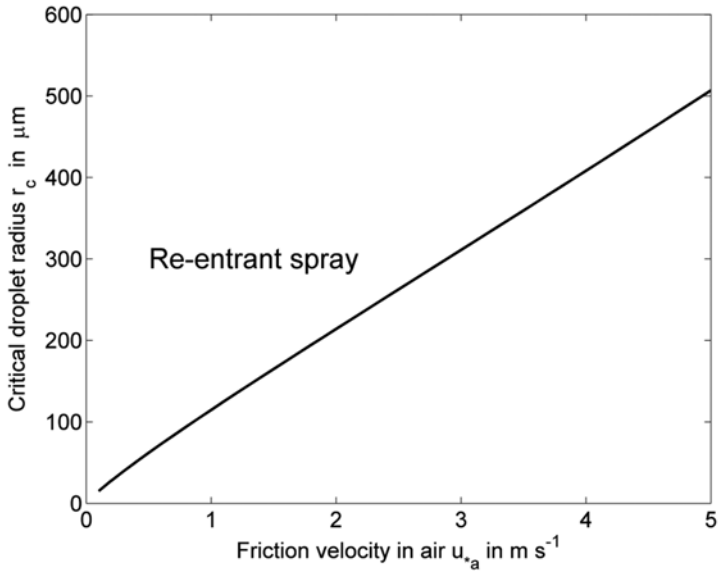

Fig. 6.17 Critical radius separating reentrant and entrained droplets according to the Barenblatt and Golitsyn (1974) theory

which means that the stratification effect reduces turbulent friction by a factor of ω^{-1}.

Equation (6.35) at $\omega = 1$ combined with the formula for the terminal velocity of raindrops (2.112) gives an equation for the droplet radius separating the two regimes according to the Barenblatt and Golitsyn theory. This critical droplet radius r_c is as follows:

$$r_c = r_v \left[1 - \ln\left(\kappa u_{*a} / w_t\right)\right]^{1/\lambda} \tag{6.39}$$

Dependence (6.39) is shown in Fig. 6.17 as a function of the friction velocity in air. Spray droplets with radii $r > r_c$ are the reentrant spray, while smaller droplets are effectively transported by turbulence. Note that for 15 m s^{-1} wind speed, which corresponds to the friction velocity in air $u_{*a} \approx 0.6$ m s^{-1}, the critical droplet radius is $r_c \approx 70$ μm. It is interesting that most of the spray generation functions shown in Fig. 6.8 reveal peaks around $r = 10^2$ μm, which may be an indication that the turbulent diffusion is not an effective mechanism for transporting these relatively large droplets. This, however, might also be an indication that the known spray generation functions underestimate the contribution of large droplets, because the largest droplets might elude detection during the measurements conducted at some distance from the sea surface.

The saturation-limited flow implies an infinite supply of particles from the boundary to the flow. If the particle supply is not infinite then at small distances

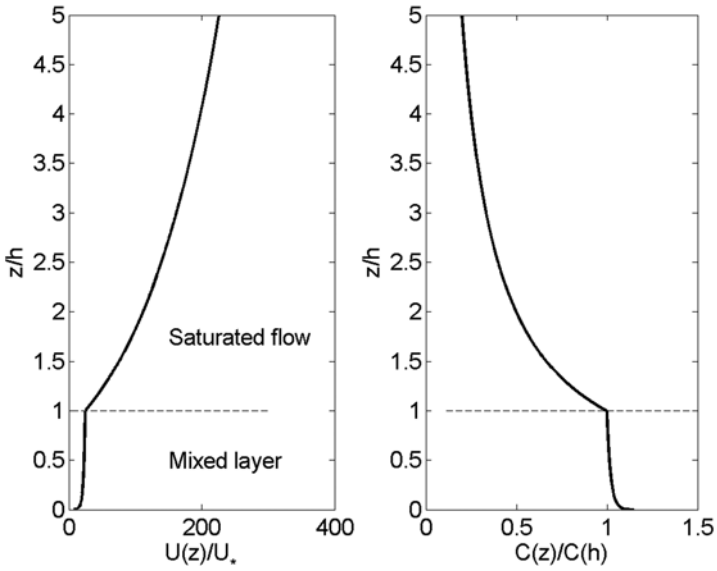

Fig. 6.18 Vertical profiles of velocity and concentration in the suspension-limited flow according to the Barenblatt and Golitsyn (1974) model

from the surface the velocity and concentration profiles follow the laws of the classic logarithmic boundary layer (6.36), while switching to the saturation-limited regime (6.37) at some distance h from the boundary. In the latter case, a new parameter enters the problem, the surface buoyancy flux of spray particles B_{sp}, and a new length scale appears:

$$L_* = \frac{u_{*a}^3}{\kappa B_{sp}}, \tag{6.40}$$

which is an analog to the Oboukhov buoyancy length scale in the thermally stratified turbulent boundary layer. A mixed layer with thickness $h \sim L_*$ would form in the atmospheric boundary layer if heat and moisture fluxes were ignored. This regime is schematically illustrated in Fig. 6.18 for $\omega = 0.1$.

The buoyancy flux due to sea spray can be estimated from the sea spray generation function (see Sect. 6.3.3) in the following way.

$$B_{sp} = -\frac{4\pi}{3}\rho g \int_{r_{lo}}^{r_{hi}} r_0^3 \frac{dF_0}{dr} dr_0, \tag{6.41}$$

where B_{sp} is in (kg m^{-3}) (m^2 s^{-3}).

A rough estimate of the Oboukhov-type length scale from (6.40) using sea spray generation function (6.20) for a 15 m s^{-1} wind speed is $L_* = -10^2$ m. The sea spray generation function dF_0/dr_0 defined from Eqs. (6.20)–(6.21) increases with friction

velocity as u_{*a}^3, which is the same dependence on friction velocity as in the numerator of Eq. (6.40). As a result, the above estimate for L_* does not change with wind speed.

According to the Monin–Oboukhov theory, the buoyancy effects are pronounced at a height $z \sim |L_*|$ and negligible for $z \langle 0.1 |L^*|$. Furthermore, length scale L^* is additive to the classical Oboukhov length scale determined by the heat and moisture fluxes in the atmospheric boundary layer, which can further diminish the buoyancy effect of sea spray.

Theoretically, the sea spray concentration in the marine boundary layer can reach the level at which the associated stratification may suppress turbulent fluctuations, reducing wind stress at the ocean surface. However, if the spray generation function (6.20)–(6.21) holds for very high wind speed conditions, then the influence of sea spray on the atmospheric boundary layer dynamics within the 10-m layer is relatively small even during hurricanes. As a result, the effect of sea spray buoyancy appears to be only marginal on the drag coefficient C_d referenced to a 10-m altitude. Sea spray buoyancy effects, nevertheless, can be more pronounced at larger altitudes (Bao et al. 2011).

6.4.3 The Air–Sea Interface Under Hurricane Conditions

Hurricanes take heat energy from the ocean and redeposit some as kinetic energy. How effective is the process of extraction of energy from the ocean and its dissipation in the ocean significantly depends on the properties and state of the sea surface.

Under low wind speed conditions, viscous stress at the air–sea interface supports the exchange of momentum between the atmosphere and ocean. Under moderate wind speed conditions, wind waves develop and the wave-induced stress becomes more important than the viscous stress. Breaking waves create whitecaps, which cover greater area with increasing wind speed. At very high wind speeds, the sea surface is dominated by streaks of foam and spray (Figs. 6.1).

Holthuijsen et al. (2012) have shown with extended analysis of observations from aerial reconnaissance films that whitecap coverage increases with wind, though, at very high wind speeds, saturates at 4% (Figs. 6.19, 6.20). The traditional assumption was that the whitecap coverage increases to 100% under hurricane conditions. However, the previous studies were limited by 23 m s^{-1} wind speed. At higher wind speeds, the "whiteout" is increasingly dominated by the streaks of foam and spray. At wind speeds above 40 m s^{-1}, the streaks merge into a whiteout with complete coverage (Fig. 6.1). The origin of whiteout is presumably a result of direct disruption of the air–sea interface by the KH and or Tollmien–Schlichting (TS) instability (Sect. 6.4.4).

The mixed-phase environment consisting of air bubbles in water and sea spray in air changes dynamics and thermodynamics of the air–sea interaction. Better understanding of the underlying physics is therefore fundamental to hurricane forecasting.

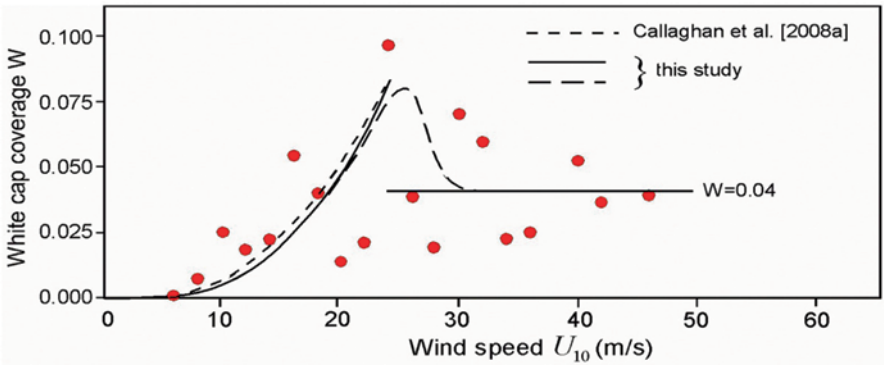

Fig. 6.19 The whitecap coverage obtained from the analysis of photos from low-level reconnaissance flights and approximated with a power law for wind speeds below 24 m s^{-1} and a constant above. A tanh capping with overshoot to a limiting value is shown with long dashes. Adapted from Holthuijsen et al. (2012). Reproduced by permission of American Geophysical Union

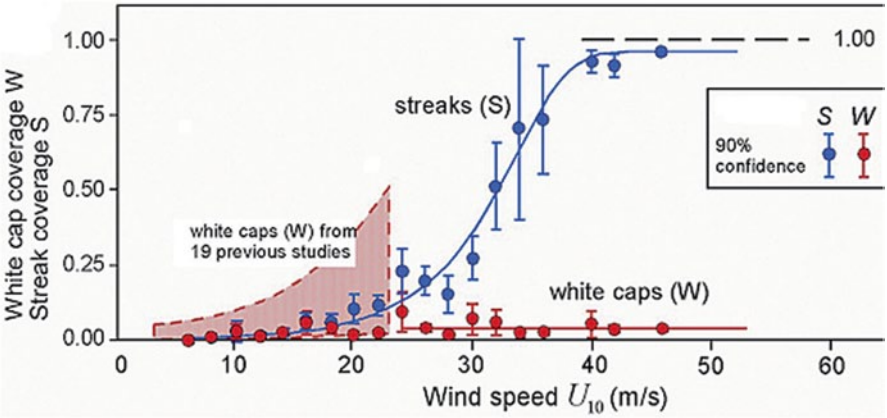

Fig. 6.20 Whitecap coverage W and streak coverage S as a function of wind speed. Blue and red dots represent observations, which are approximated with blue and red lines, respectively. Whitecap coverage W from 19 previous studies compiled by Anguelova and Webster (2006) is represented by shaded area. Adapted from Holthuijsen et al. (2012). Reproduced by permission of American Geophysical Union

6.4.4 Direct disruption of the air–sea interface

Whitecapping is not the most effective mechanism for disrupting the air–sea interface under very high wind speed conditions. More intense and widespread disruption of the interface between air and water under hurricane conditions can be achieved through the KH instability. The KH instability of the air–sea interface de-

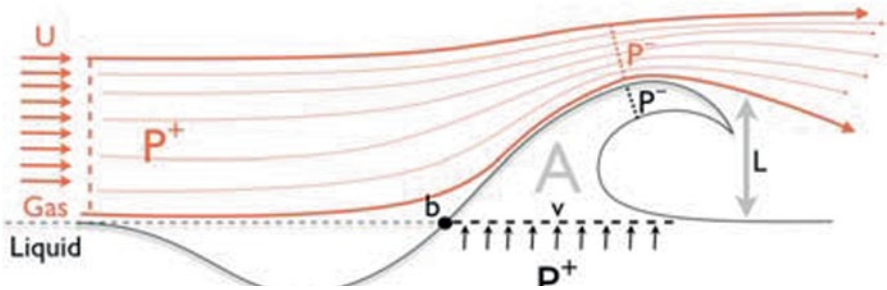

Fig. 6.21 Local perturbation of the KH instability. The wavelet that emerged due to the KH instability breaks the air–water interface when inequality (6.46) is satisfied. After Hoepffner et al. (2011). Copyright (2011) by the American Physical Society

velops within a very short time period (Kelly 1965). The TS instability (Yecko et al. 2002) is potentially another important process taking place at the air–sea interface under hurricane conditions.

The KH instability is the interfacial-type instability, while the TS instability develops in viscous sublayers in the air and/or water side. Note that similar processes take place during the atomization of liquid fuels in cryogenic and diesel engines (Yecko et al. 2002). Under hurricane conditions, the KH and TS instabilities initiate the tearing of short wavelet crests, ejection of spume, and creation of two-phase environment, with subsequent smoothing of the sea surface. The surface smoothing can explain saturation of the drag coefficient at the air–sea interface, an effect observed in the field and laboratory experiments (Powell et al. 2003; Donelan et al. 2004; Black et al. 2007; Troitskaya et al. 2010).

The KH mechanism in application to the air–sea interface is illustrated in Fig. 6.21. Acceleration of the air stream above a short wavelet induces a pressure drop across the air–water interface:

$$\Delta P = P^{+} - P^{-} = A\,\rho_a U^2 kL. \tag{6.45}$$

The pressure drop breaks up the interface if ΔP exceeds the combined restoring force of gravity and surface tension (Thomson (Lord Kelvin) 1871; Miles 1959):

$$\Delta P > \left(g\rho_w + \sigma_w k^2\right) L. \tag{6.46}$$

Here, σ_w is the surface tension, ρ_w is the water density, ρ_a is the air density, k is the wavelength, g is the acceleration due to gravity, and length scale L is proportional to the wave amplitude. The dimensionless coefficient entering Eq. (6.45) in Kelvin's theory is equal to A=1. Strictly speaking, Kelvin's wave generation theory is applicable to only infinitesimally small waves. In order to be consistent with Bernoulli's law, which is valid for finite value waves, A=2 might be more appropriate.

Combining Eqs. (6.45) and (6.46) results in the following threshold condition for the KH instability:

$$U^2 > U_{cr}^2 = A^{-1}\left(g\rho/k_m + \sigma_w k_m\right)/\rho_a = 2A^{-1}\sqrt{\sigma_w \rho g/\rho_a^2}. \tag{6.47}$$

where $k_m = \sqrt{\rho g/\sigma_w}$ is the wave number corresponding to the minimum phase speed of gravity-capillary waves. Finally, Eq. (6.47) can be expressed as follows:

$$U\Big/\left(\sigma_w \rho g/\rho_a^2\right)^{1/4} > (2/A)^{1/2}. \tag{6.48}$$

Due to appreciable change of the wind velocity with height, the interfacial velocity difference U that drives the KH instability is smaller than the wind speed at the reference height (U_{10}).

Soloviev and Lukas (2010) proposed the criteria for the KH instability at the air–water interface, using the friction velocity from the air side of the interface u_{*a} as a determining parameter, in the following way:

$$Ko = u_{*a}\Big/\left(g\sigma_w \rho/\rho_a^{\,2}\right)^{1/4}. \tag{6.49}$$

The instability occurs at $Ko > Ko_{cr}$, where $Ko_{cr} \approx 0.26$ as determined from the result of the Koga (1981) laboratory experiment, which corresponds to $U_{10} \approx 30$ m s^{-1} for air–water interface or $U_{10} \approx 25$ m s^{-1} for air–oil interface (for oil density 0.8 kg m^{-3} and air–oil surface tension 0.03 N m^{-1}).

It is easy to see that Eq. (6.49) is consistent with Eq. (6.48). However, using the friction velocity u_{*a} instead of the interfacial velocity difference U may have an advantage, since the friction velocity is related to the air–sea momentum flux ($\tau = \rho_a u_{*a}^2$), and thus can be defined in the framework of atmospheric circulation models.

Soloviev et al. (2012) demonstrated the possibility of direct disruption of the air–sea interface under hurricane force winds with an idealized 3D volume-of-fluid large eddy simulation (VOF-LES) model, which allowed simulation of the air–sea interface including effects of surface tension. For the case shown in Fig. 6.22, the wind stress $\tau = 4$ N m^{-2} (corresponding to $U_{10} \approx 40$ m s^{-1}) was applied at the upper boundary of the air layer. The Koga number $Ko = 0.38$ calculated from Eq. (6.49) in this case exceeded the critical value of $Ko_{cr} = 0.26$, which satisfied the condition for the development of the KH-type instability, $Ko > Ko_{cr}$. The disruption of the air–water interface resulted in the formation of a two-phase transition layer consisting of a fine mixture of the spray droplets and air bubbles (Fig. 6.22). The droplets in this model have densities ranging from the water density to the air density and can be interpreted as foam. Note that the model does not resolve the full size spectrum of spray droplets.

The numerical experiment with imposed short waves has demonstrated that the disruption of the air–sea interface and formation of spray take place predominantly near wave crests (Fig. 6.23). This is consistent with results of the Koga (1981) laboratory experiment where the KH-type instability of the air–water interface was observed near wave crests under hurricane force wind in the presence of an imposed monochromatic wave. The most characteristic feature of the wind–wave surface in such conditions was the appearance of small, isolated 3D projections on the air side of the interface (Fig. 6.24). Hoepffner et al. (2011) reported similar structures from a numerical simulation of the KH instability at a gas–liquid interface with relatively large (two orders of magnitude, but still one order less than air–water) density

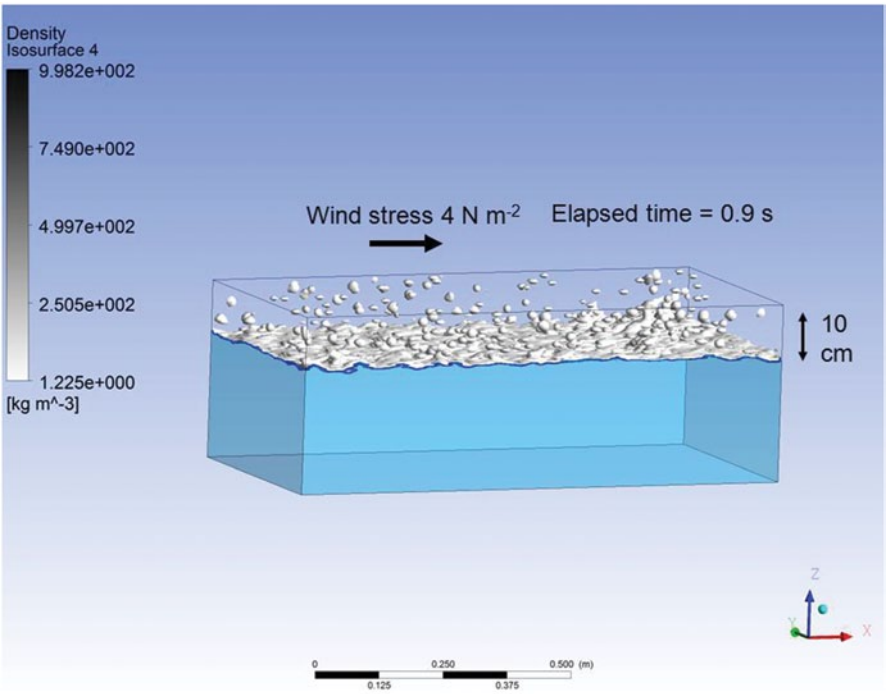

Fig. 6.22 The numerical experiment with an initially flat interface illustrates the possibility of the direct disruption of the air–water interface and formation of the two-phase environment under hurricane force wind. After Soloviev et al. (2012) by permission of John Wiley and Sons

difference. These authors observed the wave's tongue flaps that were fragile and periodically were torn into drops and thrown out to the fast gas stream. Such asymmetrical microstructure of the air–water interface is typical for the KH instability between liquids with very large density difference (e.g., the air–water interface).

Figure 6.25 shows a different view on the surface shown in Fig. 6.23, revealing intermittent streamwise structures with periodicity along the tops of wavelets. Streamwise coherent structures on the water surface in the form of streaks of spanwise size are on the order of a few centimeters wide. Similar streak-like structures have previously been reported from experiments and numerical simulations near the rigid wall (Lesieur 2008) and below the free water surface (Dhanak and Si. 1999; Tsai 2001). These streaks are subject to the TS instability. According to McNaughton and Brunet (2002), the nonlinear stage of the TS instability results in violent fluid ejections (see Fig. 5.52). The TS instability mechanism thus can contribute to the generation of spume and foam streaks in hurricane conditions.

Foam streaks are an observable feature on photographic images of the ocean surface under hurricane conditions (Fig. 6.1). At this point, however, it is difficult to conclude if the coherent structures observed in the numerical experiment (Fig. 6.25) and in the ocean are of the same nature, because the numerical model operates in

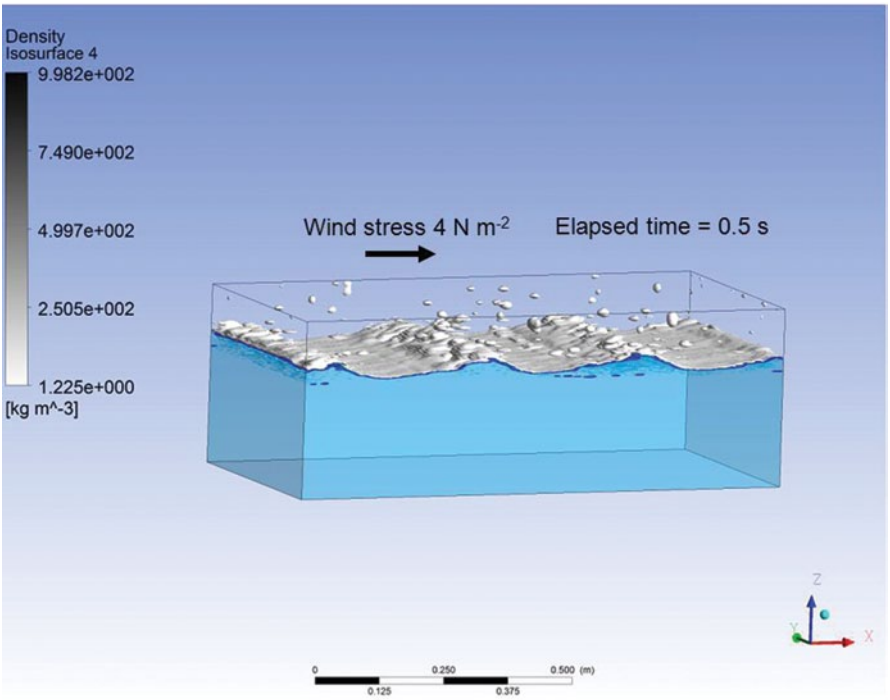

Fig. 6.23 Snapshot from a computational fluid dynamics experiment with imposed short waves demonstrates the tearing of wave crests, formation of water sheets and spume ejection into the air, 0.5 s after hurricane force wind stress is imposed at the top of the air layer. The two-phase mixture (density scale at left) of air and water covers the surface, and individual bubbles and spray droplets are also apparent. The length scale is indicated. After Soloviev et al. (2012) by permission of John Wiley and Sons

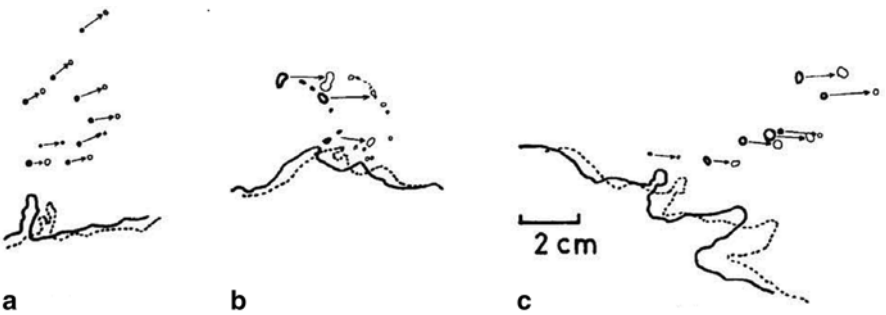

Fig. 6.24 Direct disruption of the air–water interface and production of droplets near the wave crest traced from two-color photographs in the Koga (1981) laboratory experiment at 16 m s^{-1} wind speed as measured at a reference height of 0.15 m above the water surface. Thick solid line represents first image and dotted or thin solid line represent second image. Cases **a**, **b**, and **c** represent situations at the windward slope near the crest, at the crest, and at the leading slope near the crest. After Koga (1981) by permission of Blackwell Publishing

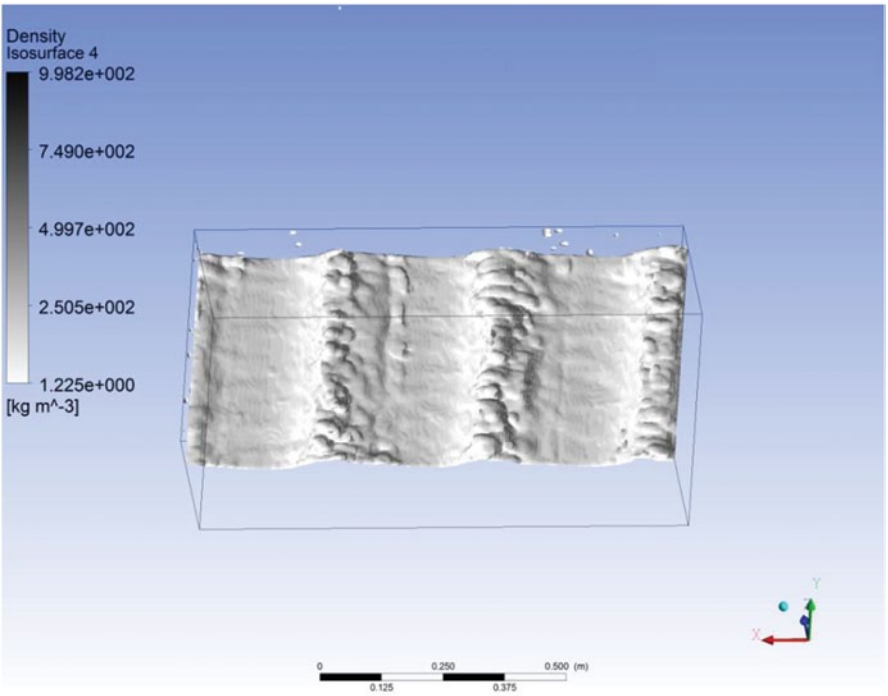

Fig. 6.25 View of the air–water surface shows quasi-periodic structures in the transverse direction along the top of wave crests. After Soloviev et al. (2012) by permission of John Wiley and Sons

a much smaller domain compared to the photo images of the sea surface shown in Fig. 6.1.

6.4.5 The Air–Sea Momentum Exchange in Very Strong Winds

The dynamics of cyclonic storms cannot be fully predicted without proper knowledge of the physical processes at the air–sea interface under high wind speed conditions. The drag coefficient formula of Large and Pond (1981) derived from field measurements, under low and moderate wind speed conditions, gives a linear increase of the drag coefficient with wind. There is evidence that this formula does not work in the high wind-speed regime. Figures 6.26 and 6.27 show the results of laboratory (Donelan et al. 2004) and in situ (Powell et al. 2003) evaluations of the drag coefficient under high wind speed conditions. Both data sets suggest that the drag coefficient does not increase (or perhaps even decreases) with wind speed starting from approximately 30 m s^{-1}.

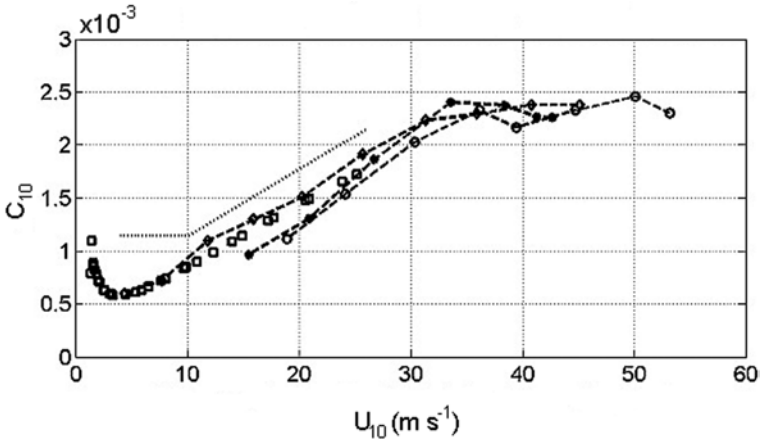

Fig. 6.26 Laboratory tank measurements of the neutral stability drag coefficient C_{10} referred to 10 m height by profile (asterisks), eddy correlation (diamonds), and momentum budget (circles) methods. The squares represent the data obtained in a different tank by Ocampo-Torres et al. (1994). The drag coefficient formula of Large and Pond (1981) derived from field measurements, under relatively low winds, is shown by dots. After Donelan et al. (2004) by permission of American Geophysical Union

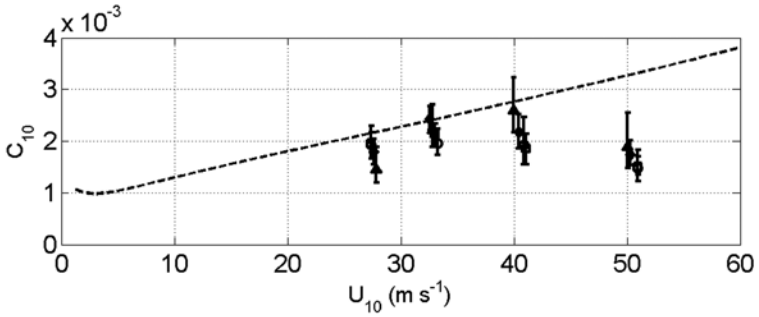

Fig. 6.27 Drag coefficient under high wind speed conditions. Dashed line is the Large and Pond (1981)-type parameterization derived by extrapolating relatively low wind speed measurements. Also shown are the experimental data of Powell et al. (2003) derived from GPS-sonde profiles and the corresponding 95% confidence limits. Reproduced with permission from Macmillan Publishers Ltd

According to the estimates described in Sect. 6.4.2, in the framework of the existing sea spray generation function, the buoyancy effect of spray by itself cannot explain the leveling off or reduction of the drag coefficient dependence on wind speed under very high wind speed conditions. Soloviev and Lukas (2010) proposed a different explanation of this effect, based on the Koga (1981) laboratory results

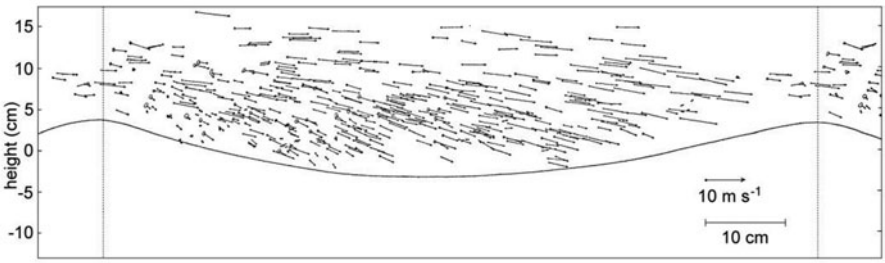

Fig. 6.28 Movements of directly produced droplets along the representative wave for the case of 16 m fetch at $u_{*a}=1.97$ m s^{-1}. Each droplet in the figure indicates actual size traced from photographs. Direction of the airflow and wave propagation is from left to right. Arrows indicate the droplet velocity vector in the coordinate system moving with the phase speed of the wave. After Koga (1981) by permission of Blackwell Publishing

that we discuss in more detail below. As discovered by Koga, the largest droplets are produced by the mechanism of direct splashing, which is initiated by the KH-type instability of the air–sea interface. Koga (1981) observed small projections, developing near wave crests where the wind stress is generally the highest and breaking up to form droplets. This observation is consistent with numerical simulations by Hoepffner et al. (2011) and Soloviev et al. (2012).

The spreading mechanism of the droplets in the Koga (1981) laboratory experiment varied according to the size of the droplets. For droplets with radius of 75 μm or more, representing the reentrant component of spray (see Fig. 6.17), the diffusion by air turbulence is not of primary importance. More important is the initial speed at the instant of the droplet production and the acceleration by wind.

Figure 6.28 shows the spatial distribution of the velocity vector of the splashing droplets relative to the wave profile in the Koga (1981) laboratory experiment. The experimental setup was able to resolve only droplets with radius larger than 0.4 mm. Most of these large droplets were produced on the leading slope near the wave crest with initial speeds of the same order, or somewhat larger than the speed of the projection (Fig. 6.24). The droplets spread upward and forward by the acceleration due to the drag of the pulsating wind flowing over the wave profile. Due to gravity, most of the droplets returned to the water surface on the windward slope near the crest of the next wave; their trajectories through the air make an angle of nearly 15 degrees with the horizontal. Most of the droplets collided with the wave surface when they were accelerated to about half the local wind speed. In some cases small droplets were jumping over the next crest, which usually took place when the steepness of the next crest was large. In this case, even large droplets sometimes jumped upward with some inclination over the next crest.

Andreas (2004) suggested that when the wind speed reaches about 30 m s^{-1}, the flux of spray droplets is equivalent to a heavy rainfall. As discussed in Chap. 2 (Sect. 2.6.5) rainfall damps some part of short surface waves, which contribute to the surface roughness and thus the drag coefficient. In analogy with rainfall, spray

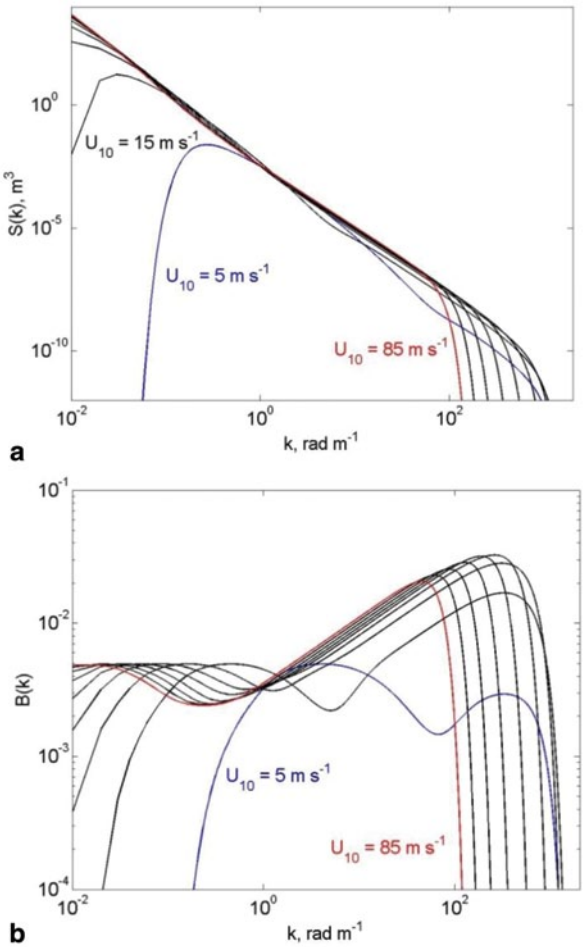

Fig. 6.29 Wave and curvature saturation spectra taking into account the suppression of short waves by two-phase environment under tropical cyclone conditions. Wind speed at a 10-m height (U_{10}) increases from 5 m s^{-1} to 85 m s^{-1} with 10 m s^{-1} increments. After Soloviev et al. (2013)

droplets generated by the KH or TS instability produce two-phase environment at the air–water interface, absorbing the energy of surface waves and smoothing the ocean surface.

Soloviev and Lukas (2010) analyzed the role of the two-phase transition layer that is formed by the reentrant spray and concluded that the two-phase environment has significant dynamic effect on short surface waves. In their conceptual framework, the two-phase environment developing at the air–sea interface eliminates a portion of the high wave number wind–wave spectrum, which is responsible for a substantial part of the air–sea drag coefficient, and thus can reduce the drag coefficient in hurricanes conditions. Furthermore, they concluded that under major

hurricane conditions (U_{10}>60 m s^{-1}), the increasing thickness of the two-phase transition layer may lead to the opposite effect—the increase of the drag coefficient limiting the maximum wind speed in tropical cyclones.

6.4.6 *Problem of Parameterization of the Air–Sea Drag Coefficient in Hurricane Conditions*

Hurricane track prediction has been steadily improving, while the intensity predictions have shown little or no progress during the last quarter century. A logical explanation of the intensity-forecasting problem comes from the method of elimination. Main factors contributing to hurricane intensity forecasting are computational power, observations, and physics. Computer performance is important for improved mesh resolution and operational forecasting. Observations contribute to the specification problem of the initial vortex initialization and the ocean–atmosphere environment and data assimilation. Physics are important for the theory of hurricanes and parameterization of unresolved spatial and temporal scales. During the last quarter century, the computer power increased by orders of magnitude and observations are now much more extensive and intense. Substantial improvements in computations and observations with no progress in intensity predictions suggest that unresolved physics are the weakest component in hurricane prediction models.

Tropical cyclone intensity is sensitive to relative strength of enthalpy and momentum fluxes between the ocean and the atmospheric boundary layer in the high wind core of the storm (Emanuel 1995). These fluxes are characterized by the corresponding air–sea exchange coefficients, C_k and C_d, which depend on the regime of air–sea interaction and the state of the air–sea interface. The laboratory experiment illustrated in Fig. 6.26 concluded that the drag coefficient increases with wind speed but levels off above approximately 33 m s^{-1} wind speed, which corresponds to the transition to a category 1 storm. Similar dependence has been obtained from field data (Fig. 6.27). This is an indication that the regime of air–sea interaction changes under tropical cyclone wind speeds. Another laboratory experiment (Jeong et al. 2012) suggests that the enthalpy exchange coefficient C_k may not have substantial dependence on wind speed.

The drag coefficient (C_d) dependence on wind speed under tropical cyclone conditions is therefore of critical importance for understanding and modeling storm intensity. In some publications, the leveling off of the drag coefficient in tropical cyclones had been linked to the suppression of near-surface turbulence by buoyancy forces due to spray loading in the atmospheric boundary layer. With the currently known sea spray generation function, the effect of sea spray buoyancy on the C_d when referred to 10 m height, however, appears to be relatively small (Soloviev and Lukas 2006; Ingel 2011; Kudrayvtsev and Makin 2011).

Soloviev et al. (2010) assumed that the change of the air–sea interaction regime under very high wind speed conditions is associated with direct disruption of the air–sea interface and formation of the two-phase transition layer consisting of air

bubbles and sea spray. However, the role of sea spray in Soloviev et al. (2010) is completely different from the explanation based on buoyancy effects. Rather, they assumed that the effect of sea spray on the air–sea drag coefficient under very high wind speed conditions is due to two-phase the transition layer suppressing short gravity-capillary waves. As a result, the relative contribution of short waves to the waveform drag gradually reduces with increasing wind speed.

Instability of the interface can be realized, for example, through the KH shear-layer instability (Kelley 1965). Our interpretation of the Kelley (1965) theoretical work is that the stochastic parametric KH instability contributes to microscale wave breaking. The microscale wave breaking as described by Banner and Phillips (1974) and Csanady (1990) is not able to disrupt the air–sea interface due to stabilizing gravity and surface tension forces. However, under very strong winds, the KH waves are able to overcome gravity and surface tension forces resulting in direct disruptions of the air–sea interface (Sect. 6.4.4). These disruptions are much more widespread than whitecapping. In addition to the interfacial-type KH instability, the TS instability taking place in the two viscous sublayers, on the water or air side of the interface, can contribute to the interface disruption. Coincidently, the air–water interface is close to the critical point where any of these instabilities can take place (Yecko et al. 2002). A result of the widespread break-up of the air–sea interface, by either KH or TS instability, is the formation of two-phase transition layer consisting of mixture of sea spray and air bubbles, which cannot support the shortest gravity-capillary waves.

Direct measurement of the gravity-capillary range of surface waves is a very difficult task under tropical cyclone conditions. Indirect data from microwave radar scattering studies appear to be helpful in verification of the wave models in the gravity-capillary range (Donelan and Pierson 1987; Bjerkaas and Reidel 1979; Apel 1994; Hwang et al. 2013). Laboratory experiments are also a valuable source of information on the dynamics of gravity-capillary waves (Jähne and Riemer 1990; Hara et al. 1994), though limited by the scale of the laboratory tank. Passive acoustic remote sensing is another potentially important source of information on the directional properties of gravity-capillary range of surface waves in the real ocean conditions, especially on the wave directional properties (Farrell and Munk 2008; Duennebier et al. 2012).

The main processes at the air–water interface that shape the long-wave component of the spectrum include wind input, nonlinear wave–wave interactions, dissipation by molecular viscosity of water, and wave breaking. The shorter wave components of the wave spectrum (the so-called high-frequencytail) are substantially determined by surface tension forces and depend on near-surface currents (Fan et al. 2009). The experimental (Hwang and Shemdin 1998) and theoretical (Banner and Mellville 1976) results reveal tendency of the high-frequency wave spectrum to saturate under high wind speed conditions, which has been incorporated in the wave model spectra of Elfouhaily et al. (1997) and Hwang et al. (2013).

Analysis based on the time-averaged wind velocity profile (Miles 1959) suggests that in the presence of wind waves, the KH instability cannot develop at the air–water interface (though can still develop at the air–oil interface). However, laboratory

(Koga 1981) and numerical (Soloviev et al. 2012) experiments, both conducted with monochromatic waves, have demonstrated that the KH instability of the air–water interface does take place, though predominantly near wave crests where the interfacial shear is higher and the local conditions for the KH instability development are more favorable. The timescale of the KH instability is much smaller than the period of energy containing wind waves (Kelley 1965). Consequently, the KH instability has sufficient time to develop within a relatively small portion of the wave period and, under very high wind speed conditions, locally disrupt the interface.

The KH mechanism is possible not only in the presence of a monochromatic surface wave but also in a more general case of the turbulent atmospheric boundary layer above the sea surface. A stochastic parametric KH instability can develop at the air–sea interface in the presence of wind waves even when it is prohibitive from the averaged air-flow conditions (Farrell and Ioannou 2008; Kudryavtsev and Makin 2011). The atmospheric boundary layer is typically turbulent and the associated characteristic wind field fluctuation is a phenomenon referred to as gustiness. Moreover, the stochastic gustiness-induced wave growth can be interpreted (Farrell and Ioannou 2008) in the framework of a generalized KH instability problem.

The Miles (1959) mechanism results in the wave growth exponential in time. It uses a linear laminar theory that has no direct role for turbulence. In the Phillips (1957) mechanism, the incoherent stochastic parametric forcing is essentially a result of the turbulence of the boundary layer. The stochastic forcing, entering additively in the Phillips theory, produces linear-in-time growth versus the exponential growth rate in the Miles theory. The stochastic forcing enters multiplicatively in the Farrell and Ioannou (2008) theory and produces an exponential growth, thus extending the Miles theory as the turbulence level increases.

Generation of wind-driven surface water waves can be interpreted as the shear stability problem in the presence of a flexible lower boundary. In the case of very high wind speed conditions, the KH instability results in extensive generation of sea spray and air bubbles. The two-phase environment suppresses short gravity-capillary waves and affects the aerodynamic drag of the sea surface under tropical cyclone conditions. Interestingly, by adding the two-phase environment under tropical cyclone conditions, we introduce substantial viscosity in the system, turning it into a rheological-type problem.

The disrupted interface cannot support very short waves. Equivalently, the dissipation of very short waves is sharply increased by turbulence associated with bubbles and spray, effectively damping such short waves. As wind speed increases, the thickness of the two-phase layer increases, eliminating increasingly longer waves in the high wave number range of the wave spectrum with consequent effect on the air–sea drag coefficient.

The bulk of the kinetic energy of surface waves is located within one-half wavelength (λ) of the surface. We correspondingly assume that the short gravity-capillary waves cannot be supported by the air–wave interface under condition $\lambda/2 < H$, where H is the thickness of the two-phase transition layer. Figure 6.30 demonstrates wave and curvature saturation spectra taking into account the suppression of short waves by two-phase environment under tropical cyclone conditions.

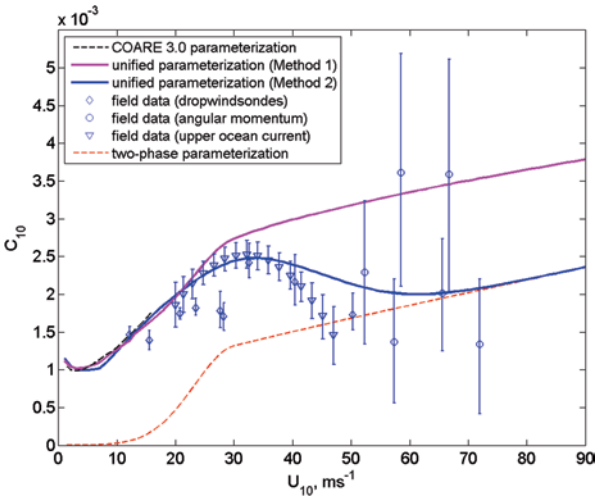

Fig. 6.30 Comparison of the unified air–sea drag parameterization calculated using Method 1 (Donelan and Person 1985) and Method 2 (Hsiao and Schemdin 1984) with the available field experiments. Field experiments (Powell et al. 2003, Black et al. 2007, Bell et al. 2012, Jarosz et al. 2012). The COARE 3.0 (Fairall et al. 2003) parameterization and two-phase (lower bound) layer parameterizations are also shown. After Soloviev et al. (2013)

Theoretical analysis of Farrell and Ioannou (2008) suggests that the stochastic parametric KH instability mechanism for the growth of surface water waves is sustained in a gusty turbulent flow above the random sea surface independently on the Miles wave generation mechanism (Miles 1959). Soloviev et al. (2013) therefore treated the waveform and two-phase layer stresses as independent entities. These stresses were then included in a unified model.

Unfortunately, the waveform stress calculation with existing theoretical models of wind–wave interaction is associated with an order of magnitude uncertainty. In operational wave models, this uncertainty is customarily compensated by introducing empirical coefficients, which are determined from field and laboratory experiments. It is, however, not clear how representative these models are under extreme, very high wind speed conditions. Furthermore, the stress due to two-phase environment at the air–sea interface, which is derived from the theoretical model, is supported by numerical simulations but has never been verified in the field.

Figure 6.30 shows calculations of the waveform stress, which are based on two different models of wind–wave interaction (Donelan and Pierson 1987 and Hsiao and Shemdin 1983, respectively). The unified parameterization denoted as "Method 1" is calculated by adding surface stresses. The unified parameterization denoted as "Method 2" operates with surface roughness length scales. We show both due to large uncertainty in the existing theories of wave generation and waveform stress estimation.

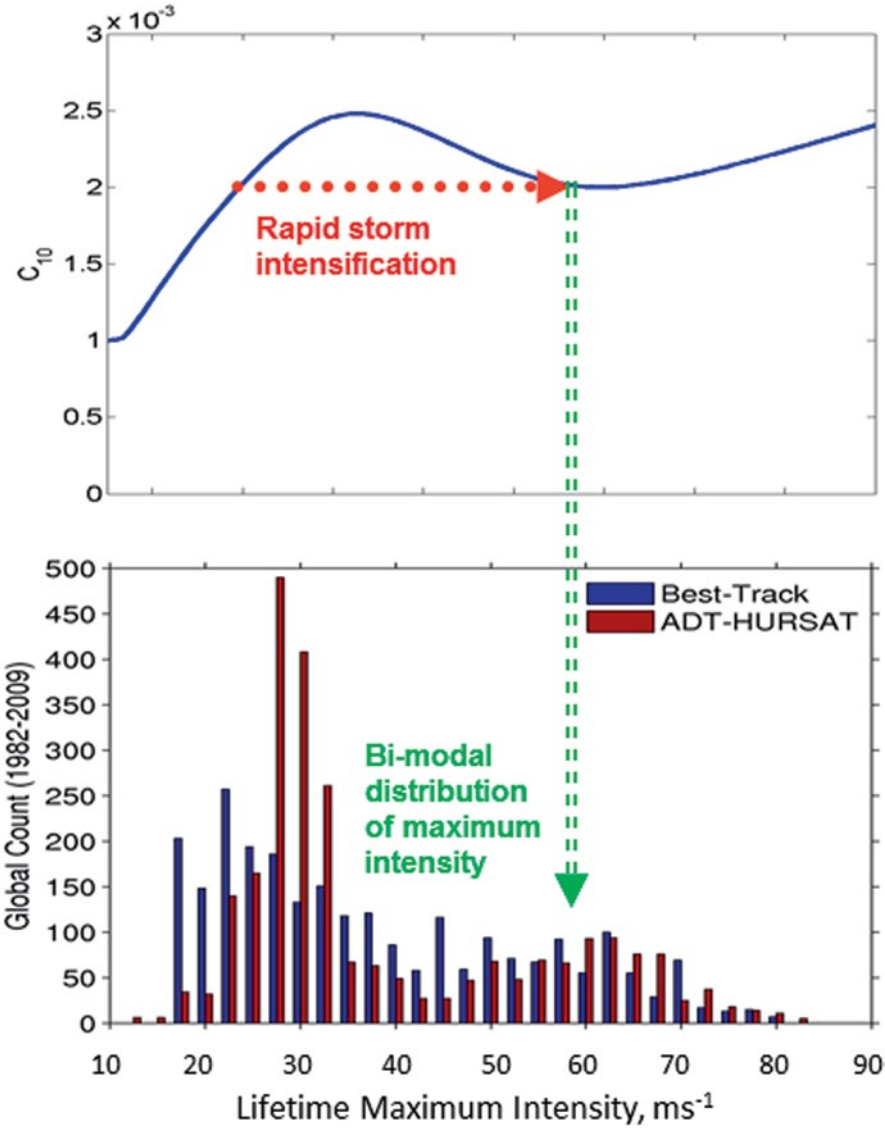

Fig. 6.31 The drag coefficient dependence on wind speed (a) may contribute to the rapid intensification from storms to major tropical cyclone and so may explain the observed (Kossin et al. 2013) bi-modal distribution of tropical cyclone intensity (b). After Soloviev et al. (2013)

The new unified drag coefficient parameterizations are compared with available data for very high wind speed conditions from field experiments. The lower bound on the drag coefficient estimates for tropical cyclone wind speeds is also shown. The unified parameterization in both cases exhibits the increase of the drag coef-

ficient with wind speed until approximately 30 m s^{-1} wind speed. Above this wind speed threshold, the drag coefficient either nearly levels off (Fig. 6.30, Method 1) or even drops and then starts again increasing above approximately 60 m s^{-1} wind speed (Fig. 6.30, Method 2). Remarkably, there is a local minimum of the drag coefficient wind speed dependence around 60 m s^{-1} for the Method 2 case.

The form of the unified parameterization reflects the fundamental change of the air–sea interface properties in tropical cyclone conditions. Here, this change is associated with the effect of direct disruption of the air–sea interface by the KH or TS instabilities, which leads to widespread production of sea spray and air bubbles. A two-phase transition layer made of a mixture of water droplets and air bubbles develops at the air–sea interface. In the model presented in this section, the two-phase environment developing at the air–sea interface eliminates some high-frequency waves, which affects the air–sea drag coefficient. With increasing wind speed, spray droplets take progressively larger potion of momentum from wind. As a result, above approximately 60 m s-1, the drag coefficient increases again with wind, which is in line with the heuristic model of Andreas (2004) discussed in Sect. 6.4.1.

The shape of the drag coefficient for high wind speeds should have consequences for hurricane dynamics and intensification. The leveling effect of the drag coefficient has been reported in a number of measurements done in the laboratory (Donelan et al. 2004) and ocean (Powell et al. 2003; Bell et al. 2012; Holthuijsen et al. 2012) during hurricane conditions. Notably, the mechanism of stochastic KH instability and the effect of two-phase environment on the short gravity-capillary waves are able to explain the leveling off of the drag coefficient (and even its reduction) under hurricane wind speeds (Fig. 6.30).

A negative slope in the C_d wind speed dependence shown in Fig. 6.30b above $U_{10} > 30$ m s^{-1} indicates that waveform drag may be reduced in certain wind speed, contributing to the rapid intensification of storms to major hurricanes. Note that the problem of rapid storm intensification has been a challenge for hurricane forecasters (Sampson et al. 2011). Despite a "sweet spot" in C_d, the subsequent slow increase of the drag coefficient with winds above 60 m s^{-1} serves as an obstacle for further intensification of a hurricane. This may explain the bimodal distribution of tropical cyclone intensity, which is an observable feature (Fig. 6.31). Other factors, however, may explain the bimodal distribution, though other explanation is also possible (Emanuel 2000).

References

Andreas EL (1992) Sea spray and the turbulent air-sea heat fluxes. J Geophys Res 97:11429–11441
Andreas EL (1998) A new sea spray generation function for wind speeds up to 32 m s^{-1}. J Phys Oceanogr 28:2175–2184
Andreas EL (2002) A review of sea spray generation function for the open ocean. In: Perrie W (ed) Atmosphere-Ocean interaction, Vol 1. WIT Press, Southampton, pp. 1–46
Andreas EL (2004) Spray stress revisited. J Phys Oceanogr 34:1429–1440

Andreas EL, Emanuel KA (2001) Effects of sea spray on tropical cyclone activity. J Geophys Res 58:3741–3751
Andreas EL, Jones KF, Fairall CW (2010) Production velocity of sea spray droplets. J Geophys Res 115:C12065
Anguelova MD, Webster F (2006) Whitecap coverage from satellite measurements: a first step toward modeling the variability of oceanic whitecaps. J Geophys Res 111:C03017
Apel JR (1994) An improved model of the ocean surface wave vector spectrum and its effects on radar backscatter. J Geophys Res 99(C8):16269–16291
Banner ML, Phillips OM (1974) On the incipient breaking of small scale waves. J Fluid Mech 65:647–656
Banner ML, Mellville WK (1976) Separation of air-flow over water waves. J Fluid Mech 77:825–842
Bao J-W, Fairall CW, Michelson SA, Bianco L (2011) Parameterizations of sea–spray impact on the air–sea momentum and heat fluxes. J Phys Oceanogr 139:3781–3797
Barenblatt GI, Golitsyn GS (1974) Local structure of mature dust storms. J Atmos Sci 31:1917–1933
Bell MM, Montgomery MT, Emanuel KA (2012) Air–sea enthalpy and momentum exchange at major hurricane wind speeds observed during CBLAST. J Atmos Sci 69:3197–3222
Bjerkaas AW, Reidel FW (1979) Proposed model for the elevation spectrum of a wind-roughened sea surface. Report APL-TG-1328–1–31, pp 31. Appl Phys Lab, Johns Hopkins University, Laurel, MD
Black PG, D'Asaro EA, Drennan WM, French JR, Niiler PP, Sanford TB, Terrill EJ, Walsh EJ, Zhang JA (2007) Air-Sea exchange in hurricanes: synthesis of observations from the coupled boundary layer air-sea transfer experiment. Bull Amer Meteor Soc 88(3):357–374
Bortkovskii RS (1983) Heat and moisture exchange between atmosphere and ocean under storm conditions. Hydrometeorological Publishing House, Leningrad, pp 160
Bowyer PA (2001) Video measurements of near-surface bubble spectra. J Geophys Res 106:14179–14190
Brooks IM, Yelland MJ, Upstill-Goddard et al (2009) Physical exchanges at the air-sea interface: field measurements from UK-SOLAS. Bull Amer Meteor Soc 90:629–644
Callaghan A, DeLeeuw G, Cohen L, O'Dowd CD (2008a) Relationship of oceanic whitecap coverage to wind speed and wind history. Geophys Res Lett 35:L23609. doi:10.1029/2008GL036165
Chamides WL, Stelson AW (1992) Aqueous-phase chemical processes in deliquescent sea-salt aerosols: a mechanism that couples the atmospheric cycles of S and sea salt. J Geophys Res 97:(20)565–20,580
Charnock H (1955) Wind stress on a water surface. Q J Roy Meteor Soc 81:639–640
Clarke AD, Owens SR, Zhou J (2006) An ultrafine sea-salt flux from breaking waves: Implications for cloud condensation nuclei in the remote marine atmosphere. J Geophys Res 111:D06202. doi:10.1029/2005JD006565
Clift R, Grace JR, Weber ME (1978) Bubbles drops and particles. Academic Press, New York, pp 380
Csanady GT (1990) The role of breaking wavelets in air-sea gas transfer. J Geophys Res 95:749–759
Deane GB (2012) Acoustic screening of the ocean surface by bubbles. Proceddings of underwater communications conference, 12–14 September 2012, Sestri Levante, Italy, p 7 (http://www.ucomms.net/proceedings.php)
Deane GB, Stokes MD (2002) Scale dependence of bubble creation mechanisms in breaking waves. Nature 418:839–844
de Leeuw G, Neele FP, Hill M, Smith MH, Vignati E (2000) Production of sea spray aerosol in the surf zone. J Geophys Res 105:(D24)29397–29409
de Leeuw G, Moerman M, Cohen L, Brooks B, Smith M, Vignati E (2003) Aerosols, bubbles and sea spray production studies during the RED experiments, Proceedings AMS conference, Long Beach, CA, 9–13 February, 2003

de Leeuw G, Andreas EL, Anguelova MD, Fairall CW, Lewis ER, O'Dowd C, Schulz M, Schwartz SE (2011) Production flux of sea spray aerosol. Rev Geophys 49:RG2001. doi:10.1029/2010RG000349

Deane GB, Stokes MD (1999) Air entrainment processes and bubble size distributions in the surf zone. J Phys Oceanogr 29:1393–1403

Dhanak MR, Si C (1999) On reduction of turbulent wall friction through spanwise wall oscillations. J Fluid Mech 383:175–195

Donelan MA, Pierson WJ (1987) Radar scattering and equilibrium ranges in wind-generated waves with application to scatterometry. J Geophys Res 92:4971–5029

Donelan MA, Haus BK, Reul N, Plant W, Stiassnie M, Graber H, Brown O, Saltzman E (2004) On the limiting aerodynamic roughness of the ocean in very strong winds. Geophys Res Lett 31:L18306

Duennebier FK, Lukas R, Nosal E-M, Aucan J, Weller RA (2012) Wind, waves, and acoustic background levels at station aloha. J Geophys Res 117:C03017

Elfouhaily T, Chapron B, Katsuros K, Vandemark D (1997) A unified directional spectrum for long and short wind-driven waves. J Geophys Res 102:15781–15796

Emanuel K (1995) Sensitivity of tropical cyclones to surface exchange coefficients and a revised steady-state model incorporating eye dynamics. J Atmos Sci 52:3969–3976

Emanuel K (2000) A statistical analysis of tropical cyclone intensity. Mon Weather Rev 128:1139–1152

Emanuel K (2003) Q similarity hypothesis for air-sea exchange at extreme wind speeds. J Atmos Sci 60:1420–1428

Fairall CW, Kepert JD, Holland GJ (1994) The effect of sea spray on the surface wind profile during conditions of strong wind. Bound -Lay Meteorol 55:305–308

Fan Y, Ginis I, Hara T (2009) The effect of wind-wave-current inter-action on air-sea momentum fluxes and ocean response in tropical cyclones. J Phys Oceanogr 39:1019–1034

Farmer DM, Li M (1995) Patterns of bubble clouds organized by Langmuir circulation. J Phys Oceanogr 25:1426–1440

Farmer DM, Vagle S, Booth AD (1998) A free-flooding acoustical resonator for measurement of bubble size distributions. J Atmos Ocean Tech 15(5):1132–1146

Farrell BF, Ioannou PJ (2008) The stochastic parametric mechanism for growth of wind-driven surface water waves. J Phys Oceanogr 38:862–879

Farrell WE, Munk W (2008) What do deep sea pressure fluctuations tell about short surface waves? Geophys Res Letters 35: L19605, doi:10.1029/2008GL035008

Garrett C, Li M, Farmer D (2000) The connection between bubble size spectra and kinetic energy dissipation rates in the upper ocean. J Phys Oceanogr 30:2163–2171

Garrettson GA (1973) Bubble transport theory with application to the upper ocean. J Fluid Mech 59:187–206

Gong SL, Barrie LA, Blanchet J-P (1997) Modeling sea-salt aerosols in the atmosphere: 1, Model development. J Geophys Res 102:3805–3818

Göz MF, Bunner B, Sommerfeld M, Tryggvason G (2001) Direct numerical simulation of bidisperse bubble swarms. Contribution to the international conference on multiphase flow, New Orleans, May 2001

Hara T, Bock EJ, Lyzenga D (1994) In situ measurements of capillary-gravity wave spectra using a scanning laser slope gauge and microwave radars. J Geophys Res 99(C6):12593–12602

Hinze JO (1955) Fundamentals of the hydrodynamic mechanism of splitting in dispersion process. AICHE J 1:289–295

Hoepffner J, Blumenthal R, Zaleski S (2011) Self-similar wave produced by local perturbation of the Kelvin-Helmholtz shear-layer instability. Phys Rev Lett 106(10):104502

Holthuijsen LH, Powell MD, Pietrzak JD (2012) Wind and waves in extreme hurricanes. J Geophys Res 117:C09003. doi:10.1029/2012JC007983

Hsiao SV, Shemdin OH (1983) Measurements of wind velocity and pressure with a wave follower during MARSEN. J Geophys Res 88:9841–9849

Hwang PA, Shemdin OH (1998) The dependence of sea surface slope on atmospheric stability and swell conditions. J Geophys Res 93:13903–13912
Hwang PA, Burrage DM, Wang DW, Wesson JC (2013) Ocean surface roughness spectrum in high wind condition for microwave backscatter and emission computations. J Atmos Oceanic Technol, in press
Iida N, Toba Y, Chaen M (1992) A new expression for the production rate of seawater droplets on the sea surface. J Oceanogr 48:439–460
Ingel LKh (2011) The effect of sea spray on the dynamics of marine atmospheric surface layer in strong winds. Izv Atmos Ocean Phys 47(1):119–127
Intergovernmental Panel on Climate Change (IPCC), Climate Change (2001) The scientific basis, contribution of working group I to the third assessment report of the intergovernmental panel on climate change. Cambridge University Press, New York
Jähne B, Riemer KS (1990) Two-dimensional wave number spectra of small-scale water surface waves. J Geophys Res 95(C7):11531–11546
Jeong D, Haus BK, Donelan MA (2012) Enthalpy transfer across the air–water interface in high winds including spray. J Atmos Sci 69:2773–2748
Johnson B, Cooke R (1979) Bubble populations and spectra in coastal waters: a photographic approach. J Geophys Res 84:3761–3766
Katsaros KB, de Leeuw G (1994) Comment on "Sea spray and turbulent air-sea heat fluxes" by Edgar L. Andreas. J Geophys Res 99:14339–14343
Keeling RF (1993) On the role of large bubbles in air-sea gas exchange and supersaturation in the ocean. J Mar Res 51:237–271
Kelly RE (1965) The stability of an unsteady Kelvin-Helmholtz flow. J Fluid Mech 22(3):547–560
Koga M (1981) Direct production of droplets from breaking wind-waves-Its observation by a multi-colored overlapping exposure technique. Tellus 33:552–563
Koga M, Toba Y (1981) Droplet distribution and dispersion process on breaking wind waves. Sci Rep Tohoku University, Sr. 5. Tohoku Geophys J 28:1–25
Kolmogorov AN (1949) O droblenii kapel v turbulentnom potoke. Dokl Akad Nauk USSR 66(15):825–828 (in Russian)
Kossin JP, Olander TL, Knapp KR (2013) Trend Analysis with a New Global Record of Tropical Cyclone Intensity. Journal of Climate, accepted
Kudryavtsev VN (2006) On the effect of sea drops on the atmospheric boundary layer. J Geophys Res 111:C07020
Kudryavtsev VN, Makin VK (2011) Impact of ocean spray on the dynamics of the marine atmospheric boundary layer. Bound -Lay Meteor 140:383–310
Large WG, Pond S (1981) Open ocean momentum flux measurements in moderate to strong winds. J Phys Oceanogr 11:324–336
Leifer I, de Leeuw G (2001) Bubble measurements in breaking-wave generated bubble plumes during the LUMINY wind-wave experiment. In: Saltzman ES, Donealn M, Drennan W, Wanninkhof R (eds) AGU monograph gas transfer at water surfaces, pp 303–309
Leifer I, de Leeuw G (2006) Bubbles generated from wind-steepened breaking waves: 1. Bubble plume bubbles. J Geophys Res 111:C06020. doi:10.1029/2004JC002673
Leifer I, de Leeuw G, Cohen LH (2000) Secondary bubble production from breaking waves: the bubble burst mechanism. Geophys Res Lett 27:4077–4080
LeMaire D, Sobieski P, Guissard A (1999) Full-range sea surface spectrum in nonfully developed state for scattering calculations. IEEE Trans Geosci, Remote Sensing 37:1038–1051
Leifer I, de Leeuw G, Cohen LH (2003) Optical measurement of bubbles: system design and application. J Atmos Oceanic Technol 20:1317–1332
Lesieur M (2008) Turbulence in fluids, fourth revised and enlarged edition. Springer. p 148.
Lewis DA, Davidson JF (1982) Bubble splitting in shear flow. Trans IChemE 60:283–291
Lewis ER, Schwartz SE (2004) Sea salt aerosol production: mechanisms, methods, measurements and models. Geophys Monogr Ser.152, pp 413, AGU, Washington, D.C
Liang J-H, McWilliams JC, Sullivan PP, Baschek B (2011) Modeling bubbles and dissolved gases in the ocean. J Geophys Res 116: C03015, doi:10.1029/2010JC006579

Liang J-H, McWilliams JC, Sullivan PP, Baschek B (2012) Large eddy simulation of the bubbly ocean: new insights on subsurface bubble distribution and bubble-mediated gas transfer. J Geophys Res 117:C04002
Lima-Ochoterena R, Zenit R (2003) Visualization of the flow around a bubble moving in a low viscosity liquid. Rev Mex Fis 49:348–352
Lohmann U, Feichter J, Penner J, Leaitch R (2000) Indirect effect of sulfate and carbonaceous aerosols: a mechanistic treatment. J Geophys Res 105:12193–12206
Marmorino GO, Trump CL (1996) High resolution measurements made across a tidal intrusion front. J Geophys Res 101(C11):25661–25674
Martinez-Bazan C, Montanes JL, Lasheras JC (1999) On the breakup of an air bubble injected into fully turbulent flow, part 2, size PDF of the resulting daughter bubbles. J Fluid Mech 401:183–207
Mårtensson EM, Nilsson ED, G de Leeuw, Cohen LH, Hansson H-C (2003) Laboratory simulations and parameterization of the primary marine aerosol production. J Geophys Res 108(D9):4297
McNaughton KG, Brunet Y (2002) Townsend's hypothesis, coherent structures and Monin-Obukhov similarity. Bound -Lay Meteor 102:161–175
Miles JW (1959) On the generation of surface waves by shear flows, part 3, Kelvin-Helmholtz instability. J Fluid Mech 6:583–598
Monahan EC, O'Muircheartaigh I (1980) Optimal power-law description of oceanic whitecap coverage dependence on wind speed. J Phys Oceanogr 10:2094–2099
Monahan EC, Fairall CW, Davidson KL, Boyle PJ (1983) Observed inter-relations between 10 m winds, ocean whitecaps and marine aerosols. Q J Roy Meteor Soc 109:379–392
Monahan EC, Spiel DE, Davidson KL (1986) A model of marine aerosol generation via whitecaps and wave disruption. In: Monahan EC, MacNiocaill G, (eds) Oceanic whitecaps and their role in air-sea exchange. D. Reidel, Dordrecht, pp 167–174
Monin AS, Krasitskii VP (1985) Phenomena on the ocean surface. Hydrometeoizdat, Leningrad, pp 376. (in Russian) Norris SJ, Brooks IM, BI. Moat BL, Yelland MJ, de Leeuw G, Pascal RW, and Brooks B (2013) Near-surface measurements of sea spray aerosol production over whitecaps in the open ocean. Ocean Sci. 9, 133-145
Ocampo-Torres FJ, Donelan MA, Merzi N, Jia F (1994) Laboratory measurements of mass transfer of carbon dioxide and water vapour for smooth and rough flow conditions. Tellus B 46: 16–32
O'Dowd CD, Smith MH (1993) Physiochemical properties of aerosols over the northeast Atlantic: evidence for wind-related submicron sea-salt aerosol production. J Geophys Res 98:1137–1149
O'Dowd CD, G de Leeuw (2007) Marine aerosol production: a review of the current knowledge. Phil Trans R Soc A 365:1753–1774. doi:10.1098/rsta.2007.2043
O'Dowd CD, Lowe JA, Smith MH (1999) Coupling sea-salt and sulphate interactions and its impact on cloud droplet concentration predictions. Geophys Res Lett 26:1311–1314
Pascal RW et al (2011) A spar buoy for high-frequency wave measurements and detection of wave breaking in the open ocean. J Atmos Oceanic Technol 28:590–605
Pattison MJ, Belcher SE (1999) Production rates of sea-spray droplets. J Geophys Res 104:18397–18407
Patro R, Leifer I, Bower P (2001) Better bubble process modeling: Improved bubble hydrodynamics parameterization. In: Saltzman ES, Donealn M, Drennan W, Wanninkhof R (eds) AGU monograph gas transfer at water surfaces pp 315–320
Phelps AD, Ramble DG, Leighton TG (1997) The use of a combination frequency technique to measure the surf zone bubble population. J Acoust Soc Am 101: 1981–1989
Phelps AD, Leighton TG (1998) Oceanic bubble population measurements using a buoy-deployed combination frequency technique. IEEE J Oceanic Eng 23:400–410
Phillips OM (1957) On the generation of waves by turbulent wind. J Fluid Mech 2:417–445
Powell MD, Vickery PJ, Reinhold TA (2003) Reduced drag coefficient for high wind speeds in tropical cyclones. Nature 422:279–283
Prandtl L (1949) Führer Durch die Strömngslehre, 3rd edn. F. Vieweg, Brawnschweig
Pruppacher HR, Klett JD (1978) Microphysics of clouds and precipitation. D. Reidel Publishing Company, Dordrecht, pp 714

Resch FR, Afeti G (1992) Sub-micron film drop production by bubbles in seawater. J Geophys Res 97:3679–3683
Sampson CR, Kaplan J, Knaff JA, DeMaria M, Sisko CA (2011) A deterministic rapid intensification aid. Wea Forecasting 26:579–585
Smith MH, Park PM, Consterdine IE (1993) Marine aerosol concentrations and estimated fluxes over the sea. Q J R Meteorol Soc 119:809–824
Soloviev A, Lukas R (2006) The Near-Surface Layer of the Ocean: Structure, Dynamics and Applications. Springer, Dordrecht, The Netherlands, 574 pp
Soloviev A, Lukas R (2010) Effects of bubbles and spray on air-sea exchange in hurricane conditions. Bound -Lay Meteorol 136:365–376
Soloviev A, Fujimura A, Matt S (2012) Air-sea interface in hurricane conditions. J Geophys Res 117:C00J34. doi:10.1029/2011JC007760
Soloviev A, Lukas R, Donelan M, Haus B, Ginis I (2013) The air-sea interface and surface stress under tropical cyclones. Nature Geoscience (manuscript for submission)
Spiel DE (1997) More on the births of jet drops from bubbles bursting on seawater surfaces. J Geophys Res 102:5815–5821
Spiel DE (1998) On the birth of film drops from bubbles bursting on seawater surfaces. J Geophys Res 103:24907–24918
Thomson W (Lord Kelvin) (1871) Hydrokinetic solutions and observations. Philosophical Magazine. Ser 4 42:pp 362–377
Thorpe SA (1986) Bubble clouds: a review of their detection by sonar, of realistic models, and of how may be determined. In: Monahan EC, MacNiocaill G (eds) Whitecaps and their role in air-sea exchange processes. D. Reidel, Norwell, pp 57–68
Thorpe SA (1982) On the clouds of bubbles formed by breaking wind-waves in deep water, and their role in air–sea gas transfer. P Trans Roy Soc Lon Ser A 304:155–210
Troitskaya YI, Sergeev DA, Kandaurov AA, Baidakov GA, Vdovin MA, and Kazakov VI (2012) Laboratory and theoretical modeling of air-sea momentum transfer under severe wind conditions. J Geophys Res. 117: C00J21, doi:10.1029/2011JC007778
Tsai W (2001) On the formation of streaks on wind-driven water surfaces. Geophys Res Lett 28(20): 3959–3962. doi:10.1029/2001GL013190.
Turner JS (1973) Buoyancy effects in fluids. Cambridge University Press, New York
Veron F, Hopkins C, Harrison EL, Mueller JA (2012) Sea spray spume droplet production in high wind speeds. Geophys Res Lett 39:L16602
Woolf DK (1993) Bubbles and the air-sea transfer velocity of gases. Atmos -Ocean 31:517–540
Woolf DK (1997) Bubbles and their role in air-sea gas exchange. In: Liss PS, Duce RA (eds) The sea surface and global change. Cambridge University Press, UK, pp 173–205
Woolf DK, Thorpe SA (1991) Bubbles and the air-sea exchange of gases in near-saturation conditions. J Mar Res 49:435–466
Black PG, D'Asaro EA, Drennan WM, French JR, Niiler PP, Sanford TB, Terrill EJ, Walsh EJ, Zhang JA (2007) Air-Sea Exchange in Hurricanes: Synthesis of Observations from the Coupled Boundary Layer Air-Sea Transfer Experiment. Bull Amer Meteor Soc 88(3): 357-374
Yecko P, Zaleski S, Fullana J-M (2002) Viscous modes in two-phase mixing layers. Phys Fluids 14:4115–4122